INTERNATIONAL JOURNAL FOR NUMERICAL METHODS IN ENGINEERING
Int. J. Numer. Meth. Engng 2010; **00**:1–26
Published online in Wiley InterScience (www.interscience.wiley.com). DOI: 10.1002/nme

A Discontinuous Galerkin Method with Plane Waves for Sound Absorbing Materials

G. Gabard[1], O. Dazel[2]

[1]*ISVR, University of Southampton, Southampton, UK*
[2]*LAUM, UMR CNRS 6613, Université du Maine, Le Mans, France*

SUMMARY

Poro-elastic materials are commonly used for passive control of noise and vibration, and are key to reducing noise emissions in many engineering applications, including the aerospace, automotive and energy industries. More efficient computational models are required to further optimise the use of such materials. In this paper we present a Discontinuous Galerkin method (DGM) with plane waves for poro-elastic materials using the Biot theory solved in the frequency domain. This approach offers significant gains in computational efficiency and is simple to implement (costly numerical quadratures of highly-oscillatory integrals are not needed). It is shown that the Biot equations can be easily cast as a set of conservation equations suitable for the formulation of the wave-based DGM. A key contribution is a general formulation of boundary conditions as well as coupling conditions between different propagation media. This is particularly important when modelling porous materials as they are generally coupled with other media, such as the surround fluid or an elastic structure. The validation of the method is described first for a simple wave propagating through a porous material, and then for the scattering of an acoustic wave by a porous cylinder. The accuracy, conditioning and computational cost of the method are assessed, and comparison with the standard finite element method is included. It is found that the benefits of the wave-based DGM are fully realised for the Biot equations and that the numerical model is able to accurately capture both the oscillations and the rapid attenuation of the waves in the porous material.

Received ...

KEY WORDS: porous material, Biot theory, discontinuous Galerkin method, plane wave

1. INTRODUCTION

The objective of this work is to develop a Discontinuous Galerkin Method (DGM) with plane waves to predict sound absorption in poro-elastic materials (PEM). Such materials are commonly used for passive control of noise and vibration. In practical applications, they are often combined as layers attached or linked to a vibrating structure or to a fluid cavity. When subjected to mechanical or acoustical excitation, they can dissipate energy through viscous, thermal and structural effects, making their computational modelling of particular importance for many engineering applications. The dynamic behaviour of porous materials is classically obtained from homogenized models and particularly from the Biot–Allard theory [1–4] which is based on a continuous field mechanics approach. The homogenized porous media is modelled as the combination of two continuous fields whose inertial and constitutive coefficients are given by phenomenological relations.

Prediction models for porous materials, by analogy with structures, are commonly classified according to three categories. The first corresponds to low frequencies for which the main computational technique is the Finite Element Method (FEM). The third category is associated

*Correspondence to: Email: olivier.dazel@univ-lemans.fr

with high frequencies where the Transfer Matrix Method provides an efficient representation of the layers of materials mentioned above. Standing between these two extremes, the second category is commonly referred to as the mid-frequency range and is currently the subject of active research. The boundaries between these regimes are somewhat arbitrary, as they depend on the properties and geometry of the porous material and of the structure it is attached to. The mid-frequencies correspond to situations where the standard FEM struggles with the size of the problem, but the statistical methods commonly used for high-frequency problems are not yet applicable. Most of the computational methods for porous materials discussed in the literature are extensions of either the low- or high-frequency methods. The method proposed in the present paper is designed for the low- and mid-frequency regimes.

Discontinuous Galerkin Methods (DGM) have been actively developed for various branches of science, especially for time-domain simulations of conservation equations, as these methods directly provide high-order, explicit schemes [5]. They generally rely on polynomial interpolations of the solution within each element, but recently the use of plane waves has been proposed. This is part of the development of so-called wave-based, or Trefftz, methods where the use of canonical solutions as basis functions improves significantly the accuracy of the numerical model, and offers exponential convergence when the number of plane waves is increased. Prominent examples of this approach include the partition of unity finite element method (PUFEM) [6], the ultra-weak variational formulation [7] and the discontinuous enrichment method [8]. The use of the discontinuous Galerkin approach in this context was then proposed using either Lagrange multipliers [9] or numerical flux methods [10]. More recently a thorough analysis of the properties of the wave-based DGM for the Helmholtz equation was conducted [11–14]. It was also shown that the DGM with numerical flux provides a unified framework to describe several wave-based methods [10, 15, 16], including the ultra-weak variational formulation, and the wave-based least-square method [17].

In this paper we present a DGM using plane waves for poro-elastic materials modelled with Biot's theory in the frequency domain. Relevant prior work include the use of a Trefftz wave-based approach [18, 19] as well as the ultra-weak formulation for the lossy wave equation [20]. The PUFEM was recently applied to an equivalent fluid model [21] and then to the full Biot equations [22]. An issue with the PUFEM is the cost of calculating the element matrices associated with numerical quadratures for highly-oscillatory integrands (it was reported in some cases that the cost of calculating the element matrices is of the same order as solving the system of linear equations). The present wave-based DGM does not suffer from this issue.

The Biot equations are introduced in the next section and it is shown that they can easily be cast as a set of conservation equations which is needed for the present DGM. In section 3 the general formulation of the wave-based DGM is recalled, and the emphasis is placed on the formulation of boundary conditions as well as coupling conditions between two different propagation media (typically between the porous medium and the surround fluid). The validation of the method is described in section 4, first for a simple wave propagating through the PEM, and then for the scattering of an acoustic wave by a porous cylinder. The accuracy, conditioning and computational cost of the method are assessed.

2. GOVERNING EQUATIONS

Throughout this paper, a harmonic time dependence $\mathrm{e}^{+\mathrm{i}\omega t}$ is assumed with the angular frequency ω. The numerical method and its applications are presented in two dimensions $(x,\, y)$. To model the propagation of waves in the porous material and in the surrounding fluid, we will consider a general system of linear conservation equations of the form:

$$\mathrm{i}\omega\mathbf{u} + \mathbf{A}_x\frac{\partial\mathbf{u}}{\partial x} + \mathbf{A}_y\frac{\partial\mathbf{u}}{\partial y} = \mathbf{0}\ , \tag{1}$$

where $\mathbf{u}$ is the vector of physical field variables whose number depends on the nature of the propagation medium. Below we consider either a porous material, or a fluid (using 8 or 3 field

DOI: 10.1002/nme

variables, respectively). The coefficient matrices $\mathbf{A}_x$ and $\mathbf{A}_y$ are assumed constant. For the porous material, these matrices are complex valued and vary with frequency ω. The conservation equations (1) represent the basis for most discontinuous Galerkin methods, and we will also use this as a starting point to formulate the proposed wave-based DGM in section 3.

2.1. First-order model for poro-elastic media

There are several formulations of the Biot equations available in the literature. In the present work we will use the Biot equations as formulated in [23] as the simplicity of this formulation greatly facilitates the algebra when deriving the plane wave basis. The only difference with [23] is that the velocity is used here instead of the displacement. The equations of motion involve the velocity $\mathbf{v}^{\mathrm{s}}$ of the solid phase of the porous material, as well as the total velocity $\mathbf{v}^{\mathrm{t}}$ of the porous material:

$$\mathrm{i}\omega\widetilde{\rho}_{\mathrm{s}} v_x^{\mathrm{s}} + \mathrm{i}\omega\widetilde{\rho}_{\mathrm{eq}}\widetilde{\gamma} v_x^{\mathrm{t}} = \frac{\partial\hat{\sigma}_{xx}}{\partial x} + \frac{\partial\hat{\sigma}_{xy}}{\partial y} \,, \tag{2a}$$

$$\mathrm{i}\omega\widetilde{\rho}_{\mathrm{s}} v_y^{\mathrm{s}} + \mathrm{i}\omega\widetilde{\rho}_{\mathrm{eq}}\widetilde{\gamma} v_y^{\mathrm{t}} = \frac{\partial\hat{\sigma}_{xy}}{\partial x} + \frac{\partial\hat{\sigma}_{yy}}{\partial y} \,, \tag{2b}$$

$$\mathrm{i}\omega\widetilde{\gamma}\widetilde{\rho}_{\mathrm{eq}} v_x^{\mathrm{s}} + \mathrm{i}\omega\widetilde{\rho}_{\mathrm{eq}} v_x^{\mathrm{t}} = -\frac{\partial p_{\mathrm{f}}}{\partial x} \,, \tag{2c}$$

$$\mathrm{i}\omega\widetilde{\gamma}\widetilde{\rho}_{\mathrm{eq}} v_y^{\mathrm{s}} + \mathrm{i}\omega\widetilde{\rho}_{\mathrm{eq}} v_y^{\mathrm{t}} = -\frac{\partial p_{\mathrm{f}}}{\partial y} \,. \tag{2d}$$

The left-hand side of these equations is related to visco-inertial terms. The PEM equivalent densities $\tilde{\rho}_{\mathrm{s}}$, $\tilde{\rho}_{\mathrm{eq}}$ and the coupling factor $\tilde{\gamma}$ are defined in [23]. The right-hand side corresponds to elastic effects. The pressure in the fluid phase is denoted p_{f}. The tensor $\hat{\boldsymbol{\sigma}}$ corresponds to the stresses in the solid phase of the porous material in the absence of fluid (i.e. *in vacuo*). These are defined as follows:

$$\mathrm{i}\omega p_{\mathrm{f}} = -\widetilde{K}_{\mathrm{eq}} \left(\frac{\partial v_x^{\mathrm{t}}}{\partial x} + \frac{\partial v_y^{\mathrm{t}}}{\partial y} \right) \,, \tag{3a}$$

$$\mathrm{i}\omega\hat{\sigma}_{xx} = \hat{A}\frac{\partial v_y^{\mathrm{s}}}{\partial y} + (\hat{A}+2N)\frac{\partial v_x^{\mathrm{s}}}{\partial x} \,, \tag{3b}$$

$$\mathrm{i}\omega\hat{\sigma}_{xy} = N \left(\frac{\partial v_x^{\mathrm{s}}}{\partial y} + \frac{\partial v_y^{\mathrm{s}}}{\partial x} \right) \,, \tag{3c}$$

$$\mathrm{i}\omega\hat{\sigma}_{yy} = (\hat{A}+2N)\frac{\partial v_y^{\mathrm{s}}}{\partial y} + \hat{A}\frac{\partial v_x^{\mathrm{s}}}{\partial x} \,. \tag{3d}$$

$\widetilde{K}_{eq}$ is the compressibility of the fluid. $\hat{A}$ and N are the elastic coefficients of the solid phase *in vacuo* which are directly obtained from the Lamé coefficients λ and μ, as shown in [23] and recalled in Appendix A.

From equations (2) and (3) it is clear that can first be cast into a non-conservative form

$$\mathrm{i}\omega\mathbf{M}\mathbf{u} + \mathbf{B}_x\frac{\partial\mathbf{u}}{\partial x} + \mathbf{B}_y\frac{\partial\mathbf{u}}{\partial y} = \mathbf{0} \,, \tag{4}$$

with the following definitions:

$$\mathbf{u} = \begin{bmatrix} v_x^{\mathrm{s}} \\ v_y^{\mathrm{s}} \\ v_x^{\mathrm{t}} \\ v_y^{\mathrm{t}} \\ \hat{\sigma}_{+} \\ \hat{\sigma}_{xy} \\ \hat{\sigma}_{-} \\ p_{\mathrm{f}} \end{bmatrix} \,, \quad \mathbf{M} = \begin{bmatrix} \widetilde{\rho}_{\mathrm{s}} & 0 & \widetilde{\gamma}\widetilde{\rho}_{\mathrm{eq}} & 0 & 0 & 0 & 0 & 0 \\ 0 & \widetilde{\rho}_{\mathrm{s}} & 0 & \widetilde{\gamma}\widetilde{\rho}_{\mathrm{eq}} & 0 & 0 & 0 & 0 \\ \widetilde{\gamma}\widetilde{\rho}_{\mathrm{eq}} & 0 & \widetilde{\rho}_{\mathrm{eq}} & 0 & 0 & 0 & 0 & 0 \\ 0 & \widetilde{\gamma}\widetilde{\rho}_{\mathrm{eq}} & 0 & \widetilde{\rho}_{\mathrm{eq}} & 0 & 0 & 0 & 0 \\ 0 & 0 & 0 & 0 & (\hat{A}+N)^{-1} & 0 & 0 & 0 \\ 0 & 0 & 0 & 0 & 0 & N^{-1} & 0 & 0 \\ 0 & 0 & 0 & 0 & 0 & 0 & N^{-1} & 0 \\ 0 & 0 & 0 & 0 & 0 & 0 & 0 & \widetilde{K}_{\mathrm{eq}}^{-1} \end{bmatrix} \,, \tag{5}$$

DOI: 10.1002/nme

and

$$\mathbf{B}_x = \begin{bmatrix} 0 & 0 & 0 & 0 & -1 & 0 & -1 & 0 \\ 0 & 0 & 0 & 0 & 0 & -1 & 0 & 0 \\ 0 & 0 & 0 & 0 & 0 & 0 & 0 & 1 \\ 0 & 0 & 0 & 0 & 0 & 0 & 0 & 0 \\ -1 & 0 & 0 & 0 & 0 & 0 & 0 & 0 \\ 0 & -1 & 0 & 0 & 0 & 0 & 0 & 0 \\ -1 & 0 & 0 & 0 & 0 & 0 & 0 & 0 \\ 0 & 0 & 1 & 0 & 0 & 0 & 0 & 0 \end{bmatrix}, \quad \mathbf{B}_y = \begin{bmatrix} 0 & 0 & 0 & 0 & 0 & -1 & 0 & 0 \\ 0 & 0 & 0 & 0 & -1 & 0 & 1 & 0 \\ 0 & 0 & 0 & 0 & 0 & 0 & 0 & 0 \\ 0 & 0 & 0 & 0 & 0 & 0 & 0 & 1 \\ 0 & -1 & 0 & 0 & 0 & 0 & 0 & 0 \\ -1 & 0 & 0 & 0 & 0 & 0 & 0 & 0 \\ 0 & 1 & 0 & 0 & 0 & 0 & 0 & 0 \\ 0 & 0 & 0 & 1 & 0 & 0 & 0 & 0 \end{bmatrix}. \tag{6}$$

The reason for introducing the non-conservative form (4) is that deriving closed-form expression of the plane-wave basis for the solution and the test functions is easier when using (4), since it provides simple links between the direct and adjoint plane wave bases, as will be shown in section 3.6. This stems from the fact that the matrices $\mathbf{B}_x$ and $\mathbf{B}_y$ are real and symmetric, while the complex-valued matrix $\mathbf{M}$ is complex symmetric (but not Hermitian).

The conservative form (1) is easily recovered from equation (4) using

$$\mathbf{A}_x = \mathbf{M}^{-1}\mathbf{B}_x, \quad \mathbf{A}_y = \mathbf{M}^{-1}\mathbf{B}_y. \tag{7}$$

For convenience we have introduced $\sigma_+ = (\hat{\sigma}_{xx} + \hat{\sigma}_{yy})/2$ and $\sigma_- = (\hat{\sigma}_{xx} - \hat{\sigma}_{yy})/2$ in the vector $\mathbf{u}$ as it simplifies the expression of the mass matrix $\mathbf{M}$ and the calculation of its inverse in (7).

It should be noted that it is also possible to formulate a DGM starting from the non-conservative form (4), provided that the numerical flux is defined in a consistent way to ensure conservation of the field variables. This approach has been derived and implemented by the authors, but it is not described in the present paper as this leads to weak forms equivalent to that obtained from the well-established DGM based on (1).

One might think that the large number of unknowns introduced in this model implies that the computational cost of solving for all these variables will be high. This is true for standard finite element methods where each variable is discretised independently, but it does not apply here. With the present wave-based method the degrees of freedom are the amplitudes of the plane waves in each element and their number is completely independent of the number of variables introduced in the governing equations.

2.2. Acoustic waves in air

To describe the acoustic waves in the fluid around the porous material we use the standard Helmholtz equation which can be written directly in the conservative form (1) by introducing the acoustic pressure p^{a} and linearised momentum $\rho_0 \mathbf{v}^{\mathrm{a}}$ as field variables:

$$\mathbf{u} = \begin{bmatrix} p^{\mathrm{a}} \\ \rho_0 v_x^{\mathrm{a}} \\ \rho_0 v_y^{\mathrm{a}} \end{bmatrix}, \quad \mathbf{A}_x = \begin{bmatrix} 0 & c_0^2 & 0 \\ 1 & 0 & 0 \\ 0 & 0 & 0 \end{bmatrix}, \quad \mathbf{A}_y = \begin{bmatrix} 0 & 0 & c_0^2 \\ 0 & 0 & 0 \\ 1 & 0 & 0 \end{bmatrix}, \tag{8}$$

where ρ_0 is the mean density and c_0 is the sound speed. This corresponds to the same set of equations used in [16].

3. WAVE-BASED DGM

We will now present the formulation and discretisation of the wave-based discontinuous Galerkin method of the conservative equations (1). We follow the same principles as in [10, 16], but the significant addition presented here is a general approach to incorporate a large class of boundary conditions (section 3.5), as well as coupling conditions between two different media (section 3.4). This approach relies heavily on the concept of characteristics which is introduced in section 3.2.

DOI: 10.1002/nme

3.1. Variational formulation

We consider a domain Ω which is represented by a set of N_e elements Ω_e. We allow for the solution $\mathbf{u}$ to be discontinuous at the interfaces between the elements. The variational formulation associated with the conservative form (1) is to find a solution $\mathbf{u}$ such that

$$\sum_e \int_{\Omega_e} \mathbf{v}_e^T \left(\mathrm{i}\omega \mathbf{u}_e + \mathbf{A}_x \frac{\partial \mathbf{u}_e}{\partial x} + \mathbf{A}_y \frac{\partial \mathbf{u}_e}{\partial y} \right) \mathrm{d}\Omega = 0 \ , \quad \forall \mathbf{v} \ , \tag{9}$$

where ^{T} denotes the Hermitian transpose. $\mathbf{u}_e = \mathbf{u}|_{\Omega_e}$ and $\mathbf{v}_e = \mathbf{v}|_{\Omega_e}$ denote the restrictions of the solution and the test function to each element Ω_e.

After integrating by parts on each element and rearranging terms we get:

$$-\sum_e \int_{\Omega_e} \left(\mathrm{i}\omega \mathbf{v}_e + \mathbf{A}_x^T \frac{\partial \mathbf{v}_e}{\partial x} + \mathbf{A}_y^T \frac{\partial \mathbf{v}_e}{\partial y} \right)^T \mathbf{u}_e \, \mathrm{d}\Omega + \sum_e \int_{\partial\Omega_e} \mathbf{v}_e^T \mathbf{F}_e \mathbf{u}_e \, \mathrm{d}\Gamma = 0 \ , \quad \forall \mathbf{v} \ , \tag{10}$$

where we have introduced the matrix $\mathbf{F}_e = \mathbf{A}_x n_x + \mathbf{A}_y n_y$ which represents the normal fluxes across the boundary of the element Ω_e. The unit normal $\mathbf{n} = (n_x, n_y)$ on the element boundary $\partial\Omega_e$ points out of the element.

A key aspect of the wave-based DGM is to use test functions $\mathbf{v}$ whose restrictions $\mathbf{v}_e$ on each elements are solutions of the adjoint problem defined on each element:

$$\mathrm{i}\omega \mathbf{v}_e + \mathbf{A}_x^T \frac{\partial \mathbf{v}_e}{\partial x} + \mathbf{A}_y^T \frac{\partial \mathbf{v}_e}{\partial y} = \mathbf{0} \ , \tag{11}$$

which is readily identified from equation (10). With this choice of test functions the integral over each element Ω_e vanishes and one is left with integrals on the interfaces between elements and on the boundary of the domain.

Secondly, we follow the usual idea from finite volume and discontinuous Galerkin methods of introducing a numerical flux on the interfaces between elements. Consider the interfaces $\Gamma_{ee'}$ between elements Ω_e and $\Omega_{e'}$, and on this interface define the unit normal $\mathbf{n}$ pointing into $\Omega_{e'}$. The field variables satisfy the conservation equations (1), and this implies that the flux $\mathbf{Fu}$ across this interface should be continuous. It follows that we can define a numerical flux $\mathbf{f}_{ee'}$ such that $\mathbf{f}_{ee'}(\mathbf{u}_e, \mathbf{u}_{e'}) = \mathbf{F}_e \mathbf{u}_e = \mathbf{F}_{e'} \mathbf{u}_{e'}$. We will discuss the choice of numerical flux in more details in section 3.3.

Finally we arrive at the following formulation of the wave-based discontinuous Galerkin methods:

$$\sum_{e,e'<e} \int_{\Gamma_{ee'}} (\mathbf{v}_e - \mathbf{v}_{e'})^T \mathbf{f}_{ee'}(\mathbf{u}_e, \mathbf{u}_{e'}) \, \mathrm{d}\Gamma + \int_{\partial\Omega} \mathbf{v}^T \mathbf{F}\mathbf{u} \, \mathrm{d}\Gamma = 0 \ , \quad \forall \mathbf{v} \ . \tag{12}$$

The boundary integrals are then modified to implement the different boundary conditions. This aspect will be discussed in more detail in section 3.4.

3.2. Characteristics

The concept of characteristics plays a central role in the analysis of partial differential equations of the form (1), see [24], and thus in the construction of numerical fluxes [25]. The basic definitions and notations are defined in this section to support the discussion of the numerical flux, boundary conditions and interface conditions in the following sections.

Consider the boundary $\partial\Omega$ with unit normal vector $\mathbf{n}$ and tangential vector $\boldsymbol{\tau}$. Through a simple change of variables we can write the governing equations (1) as

$$\mathrm{i}\omega \mathbf{u} + \mathbf{F} \frac{\partial \mathbf{u}}{\partial n} + \mathbf{T} \frac{\partial \mathbf{u}}{\partial \tau} = \mathbf{0} \ , \tag{13}$$

where $\mathbf{F}$ is the flux matrix defined above and the matrix $\mathbf{T} = -\mathbf{A}_x n_y + \mathbf{A}_y n_x$ corresponds to the flux tangential to boundary.

DOI: 10.1002/nme

These equations can be written in characteristic form by diagonalising the normal flux matrix by writing $\mathbf{F} = \mathbf{P}\mathbf{\Lambda}\mathbf{Q}$ where $\mathbf{P}$ is the matrix of eigenvectors, $\mathbf{\Lambda}$ is the diagonal matrix of eigenvalues and $\mathbf{Q} = \mathbf{P}^{-1}$. This leads to

$$\mathrm{i}\omega\tilde{\mathbf{u}} + \mathbf{\Lambda}\frac{\partial\tilde{\mathbf{u}}}{\partial n} + \mathbf{QTP}\frac{\partial\tilde{\mathbf{u}}}{\partial\tau} = \mathbf{0}\ , \quad \text{with } \tilde{\mathbf{u}} = \mathbf{Q}\mathbf{u}\ . \tag{14}$$

The components of $\tilde{\mathbf{u}}$ are the amplitudes of the characteristics. For each of the characteristics we can define the corresponding phase velocity λ in the normal direction which is given by the eigenvalues $\mathbf{\Lambda}$ of the flux matrix. For the Biot equations these eigenvalues are complex-valued, but the velocity and direction of propagation of each characteristic are easily obtained from the real part of the eigenvalue (which is consistent with group velocity). The imaginary parts of the eigenvalues represent the rates of decay of the waves. The expressions for the matrices $\mathbf{P}$, $\mathbf{Q}$ and the eigenvalues $\mathbf{\Lambda}$ are given in the Appendices A and B for the Biot equations and the wave equations, respectively.

A fundamental result obtained by Kreiss [26] for the well-posedness of linear hyperbolic problems is that the boundary conditions should be such that the incoming characteristics ($\lambda < 0$) are fully specified while the outgoing characteristics ($\lambda \geqslant 0$) are not modified. An insightful discussion of the so-called Kreiss Uniform Condition in terms of the physical properties of waves was provided by Higdon [27]. The general principle will guide the formulation of the boundary conditions and interface conditions in sections 3.4 and 3.5.

In the following it will therefore be necessary to separate the characteristics propagating in the positive or negative directions. For this purpose we introduce a notation where a superscript 0, $+$ or $-$ indicates that we retain only the characteristics with zero, positive or negative phase velocities. For instance $\tilde{\mathbf{u}}^{0+}$ contains the characteristics for which $\lambda \geqslant 0$, i.e. the characteristics propagating tangentially along the boundary $\partial\Omega$ or out of the domain. For $\mathbf{P}$ and $\mathbf{\Lambda}$ this notation applies on the columns of the matrix, for $\mathbf{Q}$ this applies to the rows of the matrix. For instance we have $\tilde{\mathbf{u}}^{0+} = \mathbf{Q}^{0+}\mathbf{u}$.

3.3. Numerical flux

A key component of the DG method is the choice of the numerical flux used at the interfaces between elements. In the present work we use the upwind flux splitting (or exact Roe solver) which is a standard numerical flux for linear hyperbolic system. The flux $\mathbf{Fu}$ on the interface can be written

$$\mathbf{Fu} = \mathbf{P}\mathbf{\Lambda}\mathbf{Q}\mathbf{u} = \mathbf{P}\mathbf{\Lambda}^{+}\mathbf{Q}^{+}\mathbf{u} + \mathbf{P}\mathbf{\Lambda}^{-}\mathbf{Q}^{-}\mathbf{u}\ , \tag{15}$$

where the diagonal matrices $\mathbf{\Lambda}^{\pm}$ only contain the positive or negative eigenvalues. The two terms on the right correspond to the distinct contributions from the characteristics propagating in the positive and negative direction, respectively.

If we now consider an interface $\Gamma_{ee'}$ between two elements, the first term in (15) is associated with the characteristics travelling from element Ω_e to $\Omega_{e'}$ and should therefore be calculated using $\mathbf{u}_e$. Conversely, the second term is associated with the characteristics travelling in the opposite direction and it is calculated using $\mathbf{u}_{e'}$. This leads directly to the following definition of the numerical flux:

$$\mathbf{f}_{ee'}(\mathbf{u}_e, \mathbf{u}_{e'}) = \mathbf{P}\mathbf{\Lambda}^{+}\mathbf{Q}^{+}\mathbf{u}_e + \mathbf{P}\mathbf{\Lambda}^{-}\mathbf{Q}^{-}\mathbf{u}_{e'}\ , \tag{16}$$

3.4. Boundary conditions

We now present a general method to introduce the boundary conditions on $\partial\Omega$ using the characteristics of the underlying equations. We consider a family of boundary conditions of the form:

$$\mathbf{Cu} = \mathbf{s}\ , \tag{17}$$

which corresponds to one or several linear constraints on the solution $\mathbf{u}$ as well as forcing terms $\mathbf{s}$.

As explained in [27], these boundary conditions should be used to specify the incoming characteristics in terms of the outgoing characteristics and the source terms, if any. So we rewrite

DOI: 10.1002/nme

equation (17) in terms of the characteristics:

$$\tilde{\mathbf{C}}\tilde{\mathbf{u}} = \mathbf{s} \;, \quad \text{with } \tilde{\mathbf{C}} = \mathbf{C}\mathbf{P} \;. \tag{18}$$

Separating the incoming characteristics from the others we get

$$\tilde{\mathbf{C}}^{-}\tilde{\mathbf{u}}^{-} = \mathbf{s} - \tilde{\mathbf{C}}^{0+}\tilde{\mathbf{u}}^{0+} \;. \tag{19}$$

As mentioned in the previous section (and discussed in detail in [27]) a well-posed boundary condition specifies completely the incoming characteristics $\tilde{\mathbf{u}}^{-}$. In other words the matrix $\tilde{\mathbf{C}}^{-}$ should be square and invertible for us to solve equation (19) and find the incoming characteristics:

$$\tilde{\mathbf{u}}^{-} = \tilde{\mathbf{R}}\tilde{\mathbf{u}}^{0+} + \tilde{\mathbf{s}}^{-} \;, \quad \text{with } \tilde{\mathbf{R}} = -(\tilde{\mathbf{C}}^{-})^{-1}\tilde{\mathbf{C}}^{0+} \;, \quad \text{and } \tilde{\mathbf{s}}^{-} = (\tilde{\mathbf{C}}^{-})^{-1}\mathbf{s} \;, \tag{20}$$

where the matrix $\tilde{\mathbf{R}}$ defines the reflection coefficients between the incoming characteristics and the others.

The remaining task is to modify the integral on $\partial\Omega$ to impose the boundary condition. We write the flux matrix $\mathbf{F} = \mathbf{P}\mathbf{\Lambda}^{0+}\mathbf{Q}^{0+} + \mathbf{P}\mathbf{\Lambda}^{-}\mathbf{Q}^{-}$ so as to isolate the contribution from the negative eigenvalues. When used in the integral on $\partial\Omega$ in (12) we get:

$$\int_{\partial\Omega} \mathbf{v}^T\mathbf{F}\mathbf{u}\,\mathrm{d}\Gamma = \int_{\partial\Omega} \mathbf{v}^T\mathbf{P}(\mathbf{\Lambda}^{0+}\tilde{\mathbf{u}}^{0+} + \mathbf{\Lambda}^{-}\tilde{\mathbf{u}}^{-})\,\mathrm{d}\Gamma \;. \tag{21}$$

Using (20) we then modify the integrand by rewritting $\tilde{\mathbf{u}}^{-}$ in terms of the other characteristics. The boundary integral then becomes

$$\int_{\partial\Omega} \mathbf{v}^T\mathbf{P}(\mathbf{\Lambda}^{0+} + \mathbf{\Lambda}^{-}\tilde{\mathbf{R}})\mathbf{Q}^{0+}\mathbf{u}\,\mathrm{d}\Gamma + \int_{\partial\Omega} \mathbf{v}^T\mathbf{P}\mathbf{\Lambda}^{-}\tilde{\mathbf{s}}^{-}\,\mathrm{d}\Gamma \;. \tag{22}$$

The second integral, which involves the source term $\tilde{\mathbf{s}}^{-}$ is part of the right-hand side. The matrix $\mathbf{P}(\mathbf{\Lambda}^{0+} + \mathbf{\Lambda}^{-}\tilde{\mathbf{R}})\mathbf{Q}^{0+}$ corresponds to the flux matrix modified so that the boundary condition (17) is imposed naturally in the variational formulation. The calculation of this matrix can be performed numerically in the implementation of the method, or can be done analytically beforehand.

We now introduced some common boundary conditions used in practice for the Biot equations (2). Note that in the case of the Biot equations we have three incoming characteristics, indicating that three boundary conditions are needed on any surface, so that the matrix $\tilde{\mathbf{C}}^{-}$ is square.

A first example of boundary conditions is when the porous material is glued to an impermeable surface, we have $\mathbf{v}^{\mathrm{s}} = \mathbf{V}$ together with $\mathbf{v}^{\mathrm{t}} \cdot \mathbf{n} = \mathbf{V} \cdot \mathbf{n}$ where $\mathbf{V}$ is the velocity of the surface. This can be written in the form (17) by defining:

$$\mathbf{C} = \begin{bmatrix} 1 & 0 & 0 & 0 & 0 & 0 & 0 & 0 \\ 0 & 1 & 0 & 0 & 0 & 0 & 0 & 0 \\ 0 & 0 & n_x & n_y & 0 & 0 & 0 & 0 \end{bmatrix} \;, \quad \mathbf{s} = \begin{bmatrix} V_x \\ V_y \\ \mathbf{V}\cdot\mathbf{n} \end{bmatrix} \;. \tag{23}$$

Another boundary condition, called sliding condition is often used. In this case, only the normal velocity is prescribed: $\mathbf{v}^{\mathrm{s}} \cdot \mathbf{n} = \mathbf{V} \cdot \mathbf{n}$ and $\mathbf{v}^{\mathrm{t}} \cdot \mathbf{n} = \mathbf{V} \cdot \mathbf{n}$. There is also no tangential stresses on the surface since the porous material is allowed to slide along the surface. This corresponds to:

$$\mathbf{C} = \begin{bmatrix} n_x & n_y & 0 & 0 & 0 & 0 & 0 & 0 \\ 0 & 0 & n_x & n_y & 0 & 0 & 0 & 0 \\ 0 & 0 & 0 & 0 & n_x^2 - n_y^2 & -2n_xn_y & 0 & 0 \end{bmatrix} \;, \quad \mathbf{s} = \begin{bmatrix} \mathbf{V}\cdot\mathbf{n} \\ \mathbf{V}\cdot\mathbf{n} \\ 0 \end{bmatrix} \;. \tag{24}$$

3.5. Interface conditions

The procedure described above for the boundary conditions can also be used for interface conditions between two different media. In our case, we will consider in the application examples, interface conditions between porous material and the fluid, or between two porous materials.

DOI: 10.1002/nme

Consider the interface $\Gamma_{ee'}$ between two elements Ω_e and $\Omega_{e'}$. The unit normal on $\Gamma_{ee'}$ points into Ω_e. The two solutions on either sides of the interface are coupled through a set of equations of the form:

$$\mathbf{C}_e \mathbf{u}_e = \mathbf{C}_{e'} \mathbf{u}_{e'} \ . \tag{25}$$

This family of coupling conditions is quite general in that we can potentially have different equations on either sides of the interfaces, implying that the unknown vectors $\mathbf{u}_e$ and $\mathbf{u}_{e'}$ can be of different sizes.

Following the same approach as in the previous sections equations (25) are rewritten in terms of the amplitudes of the characteristics:

$$\tilde{\mathbf{C}}_e \tilde{\mathbf{u}}_e = \tilde{\mathbf{C}}_{e'} \tilde{\mathbf{u}}_{e'} \ , \quad \text{with } \tilde{\mathbf{C}}_e = \mathbf{C}_e \mathbf{P}_e \ , \quad \text{and } \tilde{\mathbf{C}}_{e'} = \mathbf{C}_{e'} \mathbf{P}_{e'} \ . \tag{26}$$

We can rearrange these equations in terms of the incoming characteristics $\tilde{\mathbf{u}}_e^-$ for Ω_e and $\tilde{\mathbf{u}}_{e'}^+$ for $\Omega_{e'}$:

$$\begin{bmatrix} \tilde{\mathbf{C}}_e^- & -\tilde{\mathbf{C}}_{e'}^+ \end{bmatrix} \begin{bmatrix} \tilde{\mathbf{u}}_e^- \\ \tilde{\mathbf{u}}_{e'}^+ \end{bmatrix} = \begin{bmatrix} -\tilde{\mathbf{C}}_e^{0+} & \tilde{\mathbf{C}}_{e'}^{0-} \end{bmatrix} \begin{bmatrix} \tilde{\mathbf{u}}_e^{0+} \\ \tilde{\mathbf{u}}_{e'}^{0-} \end{bmatrix} \ . \tag{27}$$

Again, if the interface conditions (25) are well posed, the matrix $[\tilde{\mathbf{C}}_e^- \ -\tilde{\mathbf{C}}_{e'}^+]$ will be square and invertible, so that equation (27) can be solved for the incoming characteristics. A necessary condition is that the number of interface conditions corresponds to the total number of incoming characteristics on either sides of the interface. For instance in the case of the interface between a porous material and air this represents 4 equations (3 incoming characteristics for the porous material and 1 for the air). Assuming the interface conditions are well posed, equations (27) can be solved formally to write:

$$\left\{ \begin{array}{rcl} \tilde{\mathbf{u}}_e^- = & \tilde{\mathbf{R}}_e \tilde{\mathbf{u}}_e^{0+} & + \ \tilde{\mathbf{T}}_{ee'} \tilde{\mathbf{u}}_{e'}^{0-} \\ \tilde{\mathbf{u}}_{e'}^+ = & \tilde{\mathbf{R}}_{e'} \tilde{\mathbf{u}}_{e'}^{0-} & + \ \tilde{\mathbf{T}}_{e'e} \tilde{\mathbf{u}}_e^{0+} \end{array} \right. , \quad \text{with } \begin{bmatrix} \tilde{\mathbf{R}}_e & \tilde{\mathbf{T}}_{ee'} \\ \tilde{\mathbf{T}}_{e'e} & \tilde{\mathbf{R}}_{e'} \end{bmatrix} = \begin{bmatrix} \tilde{\mathbf{C}}_e^- & -\tilde{\mathbf{C}}_{e'}^+ \end{bmatrix}^{-1} \begin{bmatrix} -\tilde{\mathbf{C}}_e^{0+} & \tilde{\mathbf{C}}_{e'}^{0-} \end{bmatrix} \tag{28}$$

We have introduced the matrices $\tilde{\mathbf{R}}_e$ and $\tilde{\mathbf{R}}_{e'}$ containing the reflection coefficients and the matrices $\tilde{\mathbf{T}}_{ee'}$ and $\tilde{\mathbf{T}}_{e'e}$ containing the transmission coefficients of the characteristics.

We can now use these expressions to impose the interface conditions naturally in the variational formulations. For the formulation (12) the integrand of the boundary integral can be written:

$$\begin{aligned} \mathbf{v}_e^T \mathbf{F}_e \mathbf{u}_e - \mathbf{v}_{e'}^T \mathbf{F}_{e'} \mathbf{u}_{e'} &= \mathbf{v}_e^T (\mathbf{P}_e \mathbf{\Lambda}_e^{0+} \mathbf{Q}_e^{0+} + \mathbf{P}_e \mathbf{\Lambda}_e^- \mathbf{Q}_e^-) \mathbf{u}_e - \mathbf{v}_{e'}^T (\mathbf{P}_{e'} \mathbf{\Lambda}_{e'}^+ \mathbf{Q}_{e'}^+ + \mathbf{P}_{e'} \mathbf{\Lambda}_{e'}^{0-} \mathbf{Q}_{e'}^{0-}) \mathbf{u}_{e'} \\ &= \mathbf{v}_e^T \mathbf{P}_e (\mathbf{\Lambda}_e^{0+} \tilde{\mathbf{u}}_e^{0+} + \mathbf{\Lambda}_e^- \tilde{\mathbf{u}}_e^-) - \mathbf{v}_{e'}^T \mathbf{P}_{e'} (\mathbf{\Lambda}_{e'}^+ \tilde{\mathbf{u}}_{e'}^+ + \mathbf{\Lambda}_{e'}^{0-} \tilde{\mathbf{u}}_{e'}^{0-}) \ . \end{aligned} \tag{29}$$

Now using equation (28) we can rewrite $\tilde{\mathbf{u}}_e^-$ and $\tilde{\mathbf{u}}_{e'}^+$ in terms of the other characteristics, and the boundary integral for the variational formulation becomes

$$\int_{\Gamma_{ee'}} \mathbf{v}_e^T \mathbf{F}_e \mathbf{u}_e - \mathbf{v}_{e'}^T \mathbf{F}_{e'} \mathbf{u}_{e'} \, \mathrm{d}\Gamma = \int_{\Gamma_{ee'}} \begin{bmatrix} \mathbf{P}_e^T \mathbf{v}_e \\ \mathbf{P}_{e'}^T \mathbf{v}_{e'} \end{bmatrix}^T \begin{bmatrix} \mathbf{\Lambda}_e^{0+} + \mathbf{\Lambda}_e^- \tilde{\mathbf{R}}_e & \mathbf{\Lambda}_e^- \tilde{\mathbf{T}}_{ee'} \\ -\mathbf{\Lambda}_{e'}^+ \tilde{\mathbf{T}}_{e'e} & -\mathbf{\Lambda}_{e'}^{0-} + \mathbf{\Lambda}_{e'}^+ \tilde{\mathbf{R}}_{e'} \end{bmatrix} \begin{bmatrix} \mathbf{Q}_e^{0+} \mathbf{u}_e \\ \mathbf{Q}_{e'}^{0-} \mathbf{u}_{e'} \end{bmatrix} \mathrm{d}\Gamma \ . \tag{30}$$

To fix ideas, two different sets of conditions are presented for the interface between a porous material and air. In the first case the porous material is in direct contact with the fluid and the following conditions are applied on the interface:

$$\mathbf{v}^{\mathrm{a}} \cdot \mathbf{n} = \mathbf{v}^{\mathrm{t}} \cdot \mathbf{n} \ , \quad \text{(continuity of normal velocity)} \tag{31a}$$

$$p_{\mathrm{a}} = p_{\mathrm{f}} \ , \quad \text{(continuity of pressure)} \tag{31b}$$

$$\mathbf{n} \cdot \hat{\boldsymbol{\sigma}} \cdot \mathbf{n} = 0 \ , \quad \text{(no normal in-vacuo traction on the surface of the PEM)} \tag{31c}$$

$$\boldsymbol{\tau} \cdot \hat{\boldsymbol{\sigma}} \cdot \mathbf{n} = 0 \ , \quad \text{(no tangential in-vacuo traction on the surface of the PEM)} \tag{31d}$$

In the second example a thin impervious film covers the surface of the PEM. This thin film is an impermeable sheet covering the surface of porous material, and its mass and stiffness can be

DOI: 10.1002/nme

neglected. The corresponding coupling conditions between the air and the porous materials are as follows:

$$\mathbf{v}^{\mathrm{t}} \cdot \mathbf{n} = \mathbf{v}^{\mathrm{a}} \cdot \mathbf{n} \ , \quad \text{(continuity of normal velocity)} \tag{32a}$$

$$\mathbf{v}^{\mathrm{t}} \cdot \mathbf{n} = \mathbf{v}^{\mathrm{s}} \cdot \mathbf{n} \ , \quad \text{(continuity of normal velocity)} \tag{32b}$$

$$\mathbf{n} \cdot \hat{\boldsymbol{\sigma}} \cdot \mathbf{n} - p_{\mathrm{f}} = -p_{\mathrm{a}} \ , \quad \text{(continuity of normal stress)} \tag{32c}$$

$$\boldsymbol{\tau} \cdot \hat{\boldsymbol{\sigma}} \cdot \mathbf{n} = 0 \ , \quad \text{(continuity of normal stress)} \tag{32d}$$

It is interesting to note that the formulation introduced in this section can also be used to derive the upwind numerical flux presented in section 3.3. In the special case when the same propagation medium is present on both sides of the interface $\Gamma_{ee'}$, we can require that the flux $\mathbf{Fu}$ is continuous across this interface. This amounts to set $\mathbf{C}_e = \mathbf{C}_{e'} = \mathbf{F}$ in (25), which leads directly to equation (16). Since there is no change in material properties across the interface, the waves are completely transmitted through the interface without reflection. In equation (28), this corresponds to the matrices $\tilde{\mathbf{T}}_{ee'}$ and $\tilde{\mathbf{T}}_{e'e}$ being identity, while $\tilde{\mathbf{R}}_e$ and $\tilde{\mathbf{R}}_{e'}$ vanish.

3.6. Plane-wave discretization

Finally we introduce the use of plane waves to discretise the variational formulations (12). In each element the solution $\mathbf{u}_e$ is written as a linear combination of N_{w} plane waves:

$$\mathbf{u}_e = \sum_{n=1}^{N_{\mathrm{w}}} a_n^e \mathbf{U}_n \mathrm{e}^{-\mathrm{i}\mathbf{k}_n \cdot (\mathbf{x} - \mathbf{x}_e)} \ , \tag{33}$$

where $\mathbf{x}_e$ denotes the center of the element Ω_e while $\mathbf{k}_n$ are the wave vectors of the plane waves. The vector $\mathbf{U}_n$ defines the contribution of each plane wave on all the field variables, and specifies the phase and amplitude relations between the different variables. It corresponds to the polarisation vector used in electromagnetism. For the plane waves to be exact solution of the governing equations we have to assume that the coefficient matrices $\mathbf{A}_x$ and $\mathbf{A}_y$ are uniform over each element. With this plane-wave discretisation, the interactions between different unknowns are exactly accounted for since all the unknowns in $\mathbf{u}_e$ are approximated by the same set of plane waves. This is in contrast with most numerical methods where each unknown is discretized independently from the others.

The wavenumbers $\mathbf{k}_n$ and vectors $\mathbf{U}_n$ of the plane waves are determined by requiring that these are solutions of the governing equations (1). For a plane wave $\mathbf{u}_e = \mathbf{U}\mathrm{e}^{-\mathrm{i}\mathbf{k}\cdot\mathbf{x}}$ this corresponds to

$$(\mathbf{A}_x \cos\theta + \mathbf{A}_y \sin\theta)\mathbf{U} = \frac{\omega}{k}\mathbf{U} \ , \tag{34}$$

where k and θ are the norm and direction of $\mathbf{k}$. This simple eigenvalue problem can be solved analytically for the vector $\mathbf{U}$ and the phase velocity ω/k.

It is important to note that this eigenvalue problem is directly related to the definition of the characteristics. Equation (34) is equivalent to diagonalising the flux matrix $\mathbf{F}$ with $n_x = \cos\theta$ and $n_y = \sin\theta$. Therefore each plane wave in (33) corresponds to a specific characteristics defined along the θ direction.

It is worth reminding that the efficiency of the wave-based approach stems from the use of wavenumbers $\mathbf{k}_n$ and vectors $\mathbf{U}_n$ that are exact solution of the governing equations. The dispersion properties of the waves are exactly built into the approximation basis.

We also use a plane-wave basis for the test function $\mathbf{v}_e$:

$$\mathbf{v}_e = \sum_{n=1}^{N_{\mathrm{w}}} b_n^e \mathbf{V}_n \mathrm{e}^{-\mathrm{i}\mathbf{l}_n \cdot (\mathbf{x} - \mathbf{x}_e)} \ , \tag{35}$$

Since these test functions are solutions of the adjoint problems (11), the plane waves in the basis are defined by the following eigenvalue problem:

$$(\mathbf{A}_x^T \cos\theta + \mathbf{A}_y^T \sin\theta)\mathbf{V} = \frac{\omega}{l}\mathbf{V} \ . \tag{36}$$

DOI: 10.1002/nme

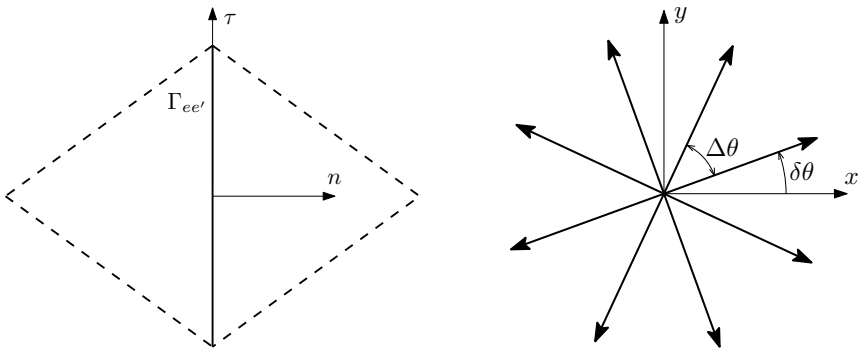

Figure 1. Left: an interface $\Gamma_{ee'}$ between two elements. Right: Example of plane wave directions for $N_{\mathrm{w}} = 8$.

Comparing (34) and (36) it is clear that $\mathbf{U}$ and $\mathbf{V}$ are the right and left eigenvectors of the same matrix $\mathbf{A}_x \cos\theta + \mathbf{A}_y \sin\theta$, it follows that $l = \overline{k}$.

In the case of the Biot equations (2–3) the calculation of the eigenvectors was found to be easier when using the non-conservative form (4). To that end, we begin by rewriting (34) and (36) as follows:

$$(\mathbf{B}_x \cos\theta + \mathbf{B}_y \sin\theta)\mathbf{U} = \frac{\omega}{k}\mathbf{M}\mathbf{U} \ , \quad (\mathbf{B}_x \cos\theta + \mathbf{B}_y \sin\theta)\overline{\mathbf{W}} = \frac{\omega}{\overline{l}}\mathbf{M}\overline{\mathbf{W}} \ , \tag{37}$$

where we have introduced the vector $\mathbf{W}$ such that $\mathbf{V} = \mathbf{M}^T\mathbf{W}$ and we have used the fact that $\mathbf{B}_x = \mathbf{M}\mathbf{A}_x$ and $\mathbf{B}_y = \mathbf{M}\mathbf{A}_y$ in (36). From (37) we can see that $\mathbf{W} = \overline{\mathbf{U}}$. As a consequence one only need to solve (37a) for the plane wave in the porous material (expressions for these can in fact be found in [4] and [23]). The plane-wave basis for the adjoint problem is then directly obtained by using $l = \bar{k}$ and $\mathbf{V} = \mathbf{M}^T\overline{\mathbf{U}}$.

In this work the N_{w} wave directions are evenly distributed between 0 and 2π as follows. This is illustrated in figure 1 and defined as $\theta_n = \delta\theta + n\Delta\theta$ with $\Delta\theta = 2\pi/N_{\mathrm{w}}$ and $n = 0, 1, ..., N_{\mathrm{w}} - 1$. $\Delta\theta$ is the angular separation between two plane waves, and $\delta\theta$ is the direction of the first plane wave.

For the Helmholtz equation, when solving (34) with (8), one finds two solutions corresponding to the acoustic wave propagating in the θ direction and the wave in the opposite direction. The third eigenvalue is $\omega/k = 0$, and it can be ignored to define the plane wave basis.

In contrast, the Biot equations (2) support three different types of waves: two compression waves (one is solid-controlled, the other one being fluid-controlled) and a shear wave propagating mainly in the solid phase. As a consequence, for each wave direction θ_n in the basis we define three distinct plane waves, each with a different pair $(\mathbf{k}_n, \mathbf{U}_n)$. For the Biot equations the number of degrees of freedom in each element is therefore $3N_{\mathrm{w}}$. While these different types of waves are represented independently within each element, all the plane waves are fully coupled at the interfaces between elements, through the numerical flux (16) and the interface condition (30), and at the boundary of the computational domain through (22).

A key benefit of the formulation (12) is the absence of integral on the elements. The integrals on the interfaces between elements can be calculated in closed form. In addition, with other wave-based methods, in particular the partition-of-unity FEM, the presence of integrands involving polynomials and exponentials requires the use of numerical quadrature methods. Since the integrands are highly-oscillatory, numerical quadrature can be very expensive. These difficulties are not present in the proposed method and the calculation of the element matrices is simple and fast.

DOI: 10.1002/nme

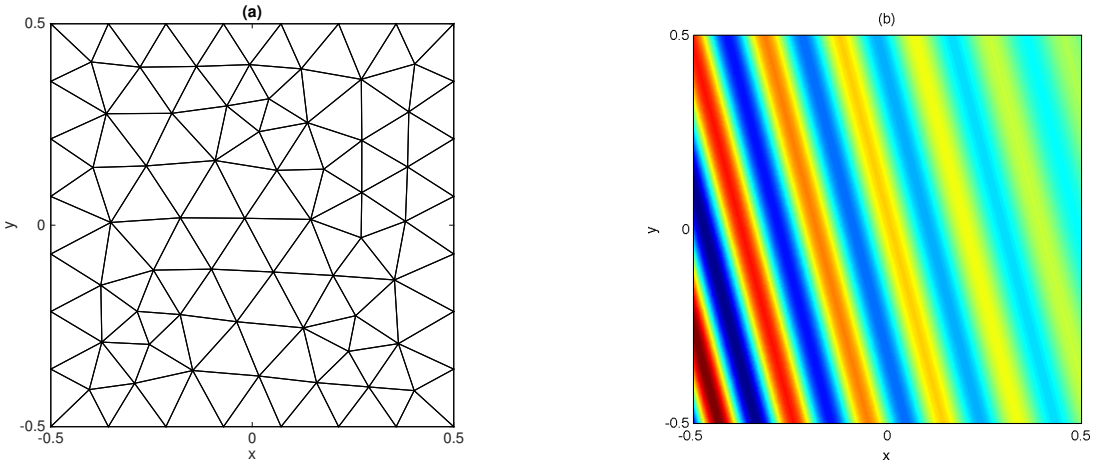

Figure 2. (a) Example of mesh with $h = 0.16$ for the square problem. (b) Example of solution p_{f} for the first compression wave with $f = 1000\,\mathrm{Hz}$ and $\theta_{\mathrm{s}} = \pi/12$.

4. VALIDATION

4.1. Plane wave propagating on a square

We first consider a benchmark problem where a single plane wave is propagating in a square computational domain, as illustrated in figure 2. This standard test case, already used in [10], is sufficiently simple to provide a detailed assessment of the performance of the method.

The square computational domain is of unit length and is discretised using an unstructured triangular mesh with elements of size h. The properties of the porous material and the fluid used in the following results are given in Appendix A. On the boundary, the incident plane wave is generated by using ghost cells. This amounts to use the numerical flux (16) on the boundary of the domain and assuming a known solution for $\mathbf{u}_{e'}$ in the form of a plane wave:

$$\mathbf{u}_{e'} = \mathbf{U}\mathrm{e}^{-\mathrm{i}kx\cos\theta_{\mathrm{s}} - \mathrm{i}ky\sin\theta_{\mathrm{s}}}\,,$$

where θ_{s} is the direction of the incident plane wave. The vector amplitude $\mathbf{U}$ and wavenumber k of this plane wave are directly obtained from (34) with $\theta = \theta_{\mathrm{s}}$ (in fact $\mathbf{U}$ will correspond to one of the columns of $\mathbf{P}^{+}$ in equation (44) with n_x and n_y substituted by $\cos\theta_{\mathrm{s}}$ and $\sin\theta_{\mathrm{s}}$, respectively). For the incoming wave we can therefore vary its frequency and direction, and choose between the two compression waves and the shear wave.

The accuracy of the numerical solution is measured by the relative error in the L^2 norm:

$$\varepsilon = \left(\int_{\Omega} |f - \hat{f}|^2 \,\mathrm{d}\Omega\right)^{1/2} \Big/ \left(\int_{\Omega} |f|^2 \,\mathrm{d}\Omega\right)^{1/2}$$

where f denotes the exact solution and $\hat{f}$ is the numerical solution. The field f will refer to either the acoustic pressure p_{f} or the solid velocity $\mathbf{v}^{\mathrm{s}}$. The computational cost of the method is measured in terms of number of degrees of freedom, but also in terms of number of non-zero entries in the algebraic system, the latter being a more accurate measure of the cost of solving the sparse linear system.

We begin by considering the effect of the incident wave direction relative to other plane waves in the basis (33) as this has a profound impact on the accuracy of the method. This can be seen by fixing the incident wave direction $\theta_{\mathrm{s}} = 0$ and changing the orientation of the plane wave basis by varying $\delta\theta$. Figure 3 shows the results for the first compression wave and for the shear wave. For this test case the exact solution is also a plane wave, and we can see that the error induced by the plane wave interpolation drops to zero whenever the incident wave direction θ_{s} coincides with one of the plane waves in the basis. This indicates that for solutions with well defined propagation directions

DOI: 10.1002/nme

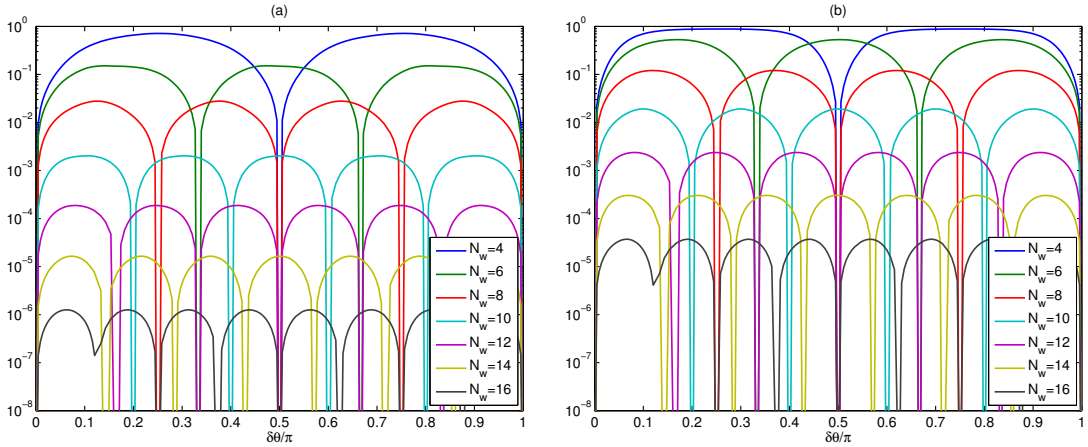

Figure 3. Numerical error as a function of the orientation $\delta\theta$ of the plane wave basis with (a) the relative L^2 error ε on p_f for the first compression wave, and (b) the relative L^2 error ε on $\mathbf{v}$ for the shear wave. Parameters are $\theta_\mathrm{s} = 0$, $f = 1000\,\mathrm{Hz}$ and $h = 0.1$.

the accuracy of the wave-based models will vary strongly with the choice of plane waves in the basis. In general it is only when multiple scattering occur that the sound field can be considered to contain a wide range of propagation directions.

As a consequence, in the remainder of this section, we will always consider the worst-case scenario by adjusting $\delta\theta$ so that the incident plane wave is half-way between two plane waves in the basis. In other words, by setting $\delta\theta = \theta_\mathrm{s} + \pi/N_\mathrm{w}$ we will observe the largest numerical error, and this provides an upper bound on the numerical error expected for a complex sound field composed of a variety of plane waves.

Also clearly visible in figure 3 is the consistent reduction in error achieved by increasing the number of plane waves in the basis. Like many other spectral methods, wave-based methods exhibit an exponential rate of convergence with respect to the number N_w of plane waves in the basis [6, 7, 10, 17]. As expected this property is also observed for the present method, as shown in figure 4. The numerical error decreases exponentially as N_w is increased (with the exception of $N_\mathrm{w} = 16$ for which the conditioning is poor). Also interesting to note in figure 4 is the slight difference in error levels between odd and even numbers of plane waves. It has been noted elsewhere that the approximation properties may differ when using an odd or even number of plane waves [28].

We now turn to the h convergence of the method by keeping the frequency fixed and progressively refining the mesh. The results are shown in figure 5 for a compression wave and the shear wave. The increase in the rate of convergence with h as more plane waves are included in the basis is obvious. For instance in figure 5a, with just four elements along the side of the square domain (corresponding to $h = 1/4$), an error of 1% can be achieved with $N_\mathrm{w} = 14$ plane waves. Additionaly, for $h = 0.1$ adding 2 more plane waves in the basis yield a reduction of the numerical error by an order of magnitude. When considering such coarse meshes, sudden changes in the element sizes can appear as h is varied since any mesh generator will have to introduce elements of size different from h for a coarse mesh. These changes in actual element size induce the oscillations seen in the convergence curves for $1/h < 12$. Note also that the high level of accuracy is also maintained for the second compression wave which is very strongly attenuated, see figure 5b. This shows that the wave-based DGM is able to describe very accurately both the propagation and the attenuation of the waves, in a way similar to that reported for the Partition of Unity FEM [21, 22].

We also include results demonstrating the convergence of the model with respect to frequency, see figure 6. When varying the frequency the properties of the porous material change, so the results in figure 6 cover a range of material properties. A coarse mesh with $h = 0.1$ is used. As expected, the numerical error decreases rapidly as the frequency is reduced (i.e. as the wavelength increases) until the conditioning deteriorates at levels of error of the order of $10^{-6}\,\%$. Interestingly even when

DOI: 10.1002/nme

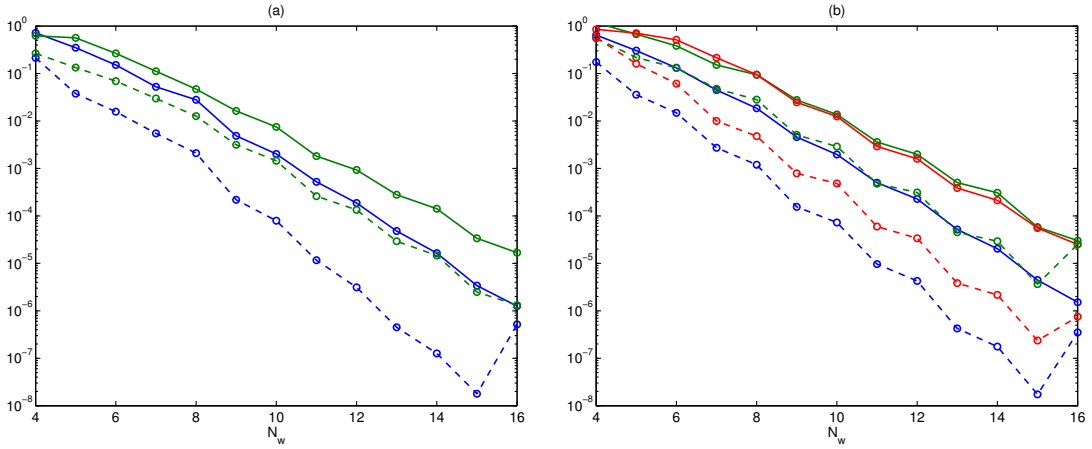

Figure 4. Relative L^2 error ε on (a) p_{f} or (b) $\mathbf{v}^{\mathrm{s}}$ as a function of the number N_{w} of plane waves in the basis, for the first compression wave (blue), the second compression wave (green) and the shear wave (red). Two frequencies are considered: 500 Hz (dashed lines) and 1000 Hz (solid lines).

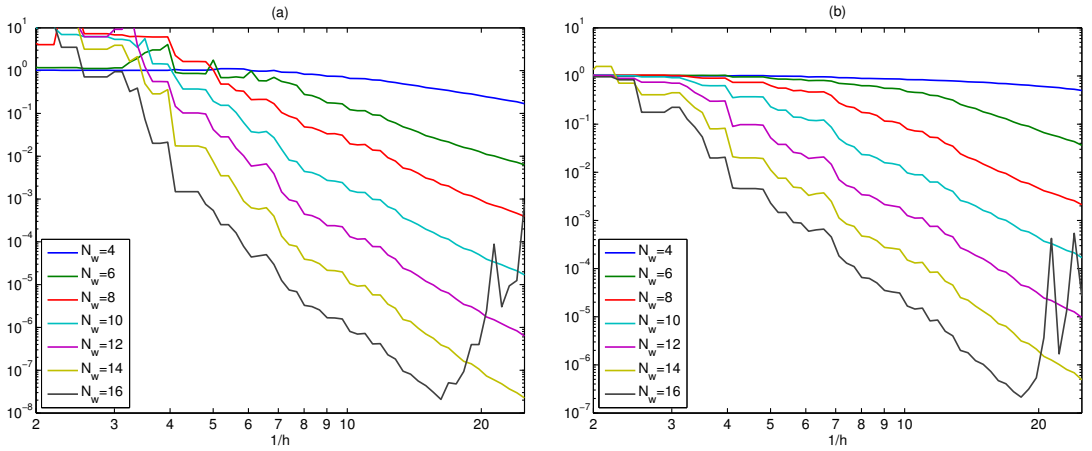

Figure 5. Convergence with the mesh resolution: (a) relative L^2 error ε on p_{f} for the first compression wave, (b) relative L^2 error ε on $\mathbf{v}^{\mathrm{s}}$ for the shear wave. Parameters are $\theta_{\mathrm{s}} = 0$, $f = 1000\,\mathrm{Hz}$, $\delta\theta = \pi/N_{\mathrm{w}}$.

the model is ill-conditioned the relative numerical error remains below 1%. The rate of convergence can be estimated from the graphs in figure 6. It was observed that for all three types of waves the order of convergence with frequency (in L^2 norm) is given by $p = \lfloor (N_{\mathrm{w}} - 1)/2 \rfloor - 1/2$, which is consistent with that reported by Cessenat and Després for the UWVF [7].

Finally, for wave-based methods it is important to assess the conditioning of the numerical models. The condition number of the algebraic system is shown in figure 7 either as a function of the frequency or the numerical error. The conditioning is seen to deteriorate rapidly as the frequency decreases or as the number of plane waves in the basis is increased. The rate at which the condition number decreases with frequency is increasing with N_{w}, in a manner similar to the accuracy of the model assessed in figures 5 and 6. The very high condition numbers observed at low frequency and/or for a large number of plane waves is responsible for the loss of convergence observed in figures 5 and 6.

However, figure 7b shows that the accuracy and the conditioning are very closely correlated, almost independently of the number of plane waves. This means that for a fixed accuracy, increasing N_{w} will increase the efficiency of the calculation, with only a moderate impact on the conditioning

DOI: 10.1002/nme

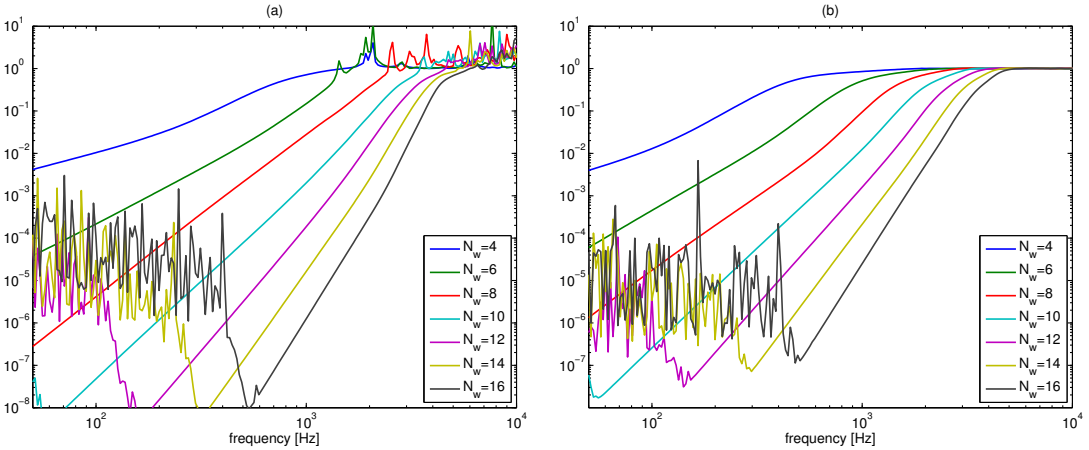

Figure 6. Convergence with frequency: (a) relative L^2 error ε on p_f for the first compression wave, (b) relative L^2 error ε on $\mathbf{v}^\mathrm{s}$ for the shear wave. Parameters are $\theta_\mathrm{s} = 0$, $h = 0.1$, $\delta\theta = \pi/N_\mathrm{w}$.

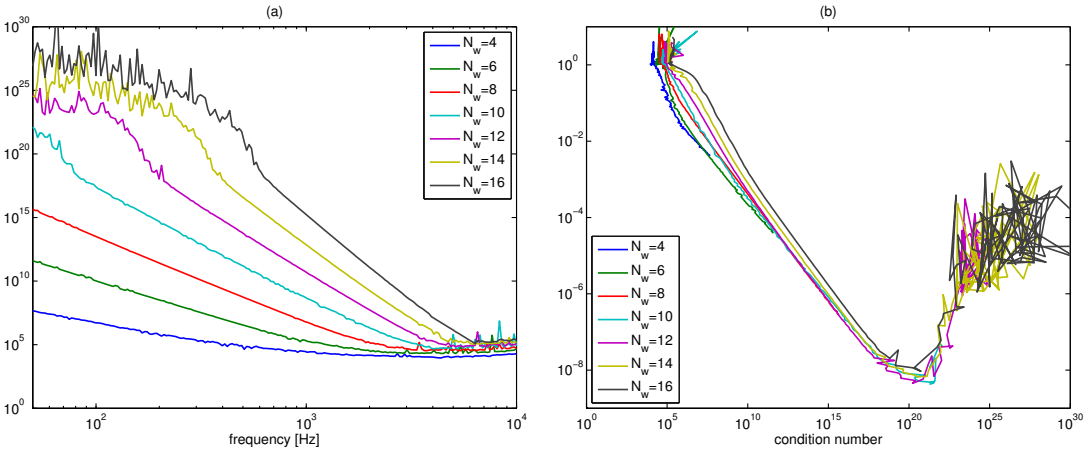

Figure 7. Conditioning of the numerical model for the first compression wave with a mesh resolution $h = 0.1$. (a) Condition number as a function of frequency. (b) Relative error ε on p_f as a function of the condition number.

of the system. This also suggests that controlling the conditioning is potentially a good way to control the accuracy.

4.2. Comparison with standard finite elements

Numerical predictions for waves in porous material almost always rely on standard finite elements [29–32]. We now compare the wave-based DGM against the standard finite element method with quadratic shape functions. The FEM is based on the first $(\mathbf{u}, p)$ formulation by Atalla *et al.* [29]. In this 2D problem, each node is associated to three degrees of freedom, two displacement components and the acoustic pressure. An excitation of the compression wave in the solid is considered with $\theta_s = 0$.

The first example, presented in Figure 8, corresponds to a simulation at a fixed frequency $f = 1\,\mathrm{kHz}$. For both the DG and FE methods, the convergence is achieved by mesh refinement. Figure 8a presents the convergence in terms of degrees of freedom and 8b in terms of non-zero entries in the matrix of the problem. Refining the mesh for the finite element method yields only a slow reduction in the absolute level of error but not a change in the rate of convergence (as expected from h-convergence). Overall it appears that the quadratic finite elements offer a level of accuracy

DOI: 10.1002/nme

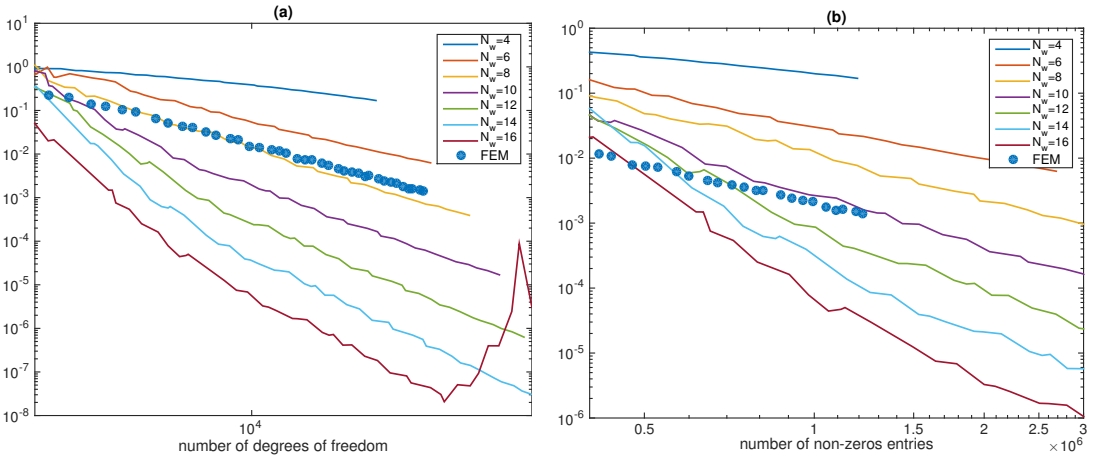

Figure 8. Relative L^2 error ε on p_f for the compression wave in the solid as a function of (a) the number of degrees of freedom, (b) the number of non-zero entries in the matrix. Parameters are $\theta_\mathrm{s} = 0$, $f = 1\,\mathrm{kHz}$, $\delta\theta = \pi/N_\mathrm{w}$.

comparable to the wave-based DGM with $N_\mathrm{w} = 8$ when they are compared in terms of degrees of freedom and $N_\mathrm{w} = 10$ when they are compared in terms of non-zero entries.

Similar conclusions can be obtained when considering the convergence with frequency presented in Figure 9. The mesh resolution for the wave-based DGM is fixed at $h = 0.1$ corresponding to $N_\mathrm{e} = 328$ elements. Several DGM results are presented corresponding to different numbers N_w of plane waves per element, each of these corresponding to a total number of degrees of freedom given by $N_\mathrm{e}N_\mathrm{w}$. To provide a valid comparison, different meshes were created for the FE model such that each mesh leads to a number of degrees of freedom close to $N_\mathrm{e}N_\mathrm{w}$. In this way, for each value of N_w for the DG model, we have a corresponding FE model with a similar number of degrees of freedom. With the DGM, the ability to increase the number of plane waves allows for a drastic improvement in accuracy compared to the standard FE model. The benefit of the wave-based DG compared to the finite element method currently in use for waves in porous material is therefore quite obvious in Figure 9. It should be noted that, to really compete with the wave-based method, a finite element method with high-order shape functions could be considered, but this is well beyond the scope of this paper.

4.3. Sound absorption by a thin poroelastic layer

We now consider the absorption of sound by a thin layer of poroelasic material clamped to a rigid wall. The properties of the layer are given in Table I and correspond to Mat. B which is a real material previously characterised. This layer, of $3\,\mathrm{cm}$ thickness, is excited by an airborne plane wave with a angle of incidence of 45 degrees. It is possible to obtain an closed-form expressions for the reflection coefficient and the absorption coefficient. Their dependence with frequency is shown in Figure 10a. Frame resonances can be observed at $402\,\mathrm{Hz}$ and at $1235\,\mathrm{Hz}$. For these frequencies, the equivalent fluid or limp model are not accurate because there is a strong coupling between the fluid and solid phases and it is necessary to model the problem with the full Biot theory. The second resonance will be used to check the validity of the numerical scheme.

This problem is solved numerically using the standard FEM and the proposed DGM scheme. In these simulations, the lateral dimension of the layer is $1\,\mathrm{m}$ so that the sample is representative of thin layers used in industrial applications. The computational domain only includes the porous region. Instead of numerically solving for the propagation of sound in the air above the porous layer, the incident plane wave and the reflected wave are represented exactly but the amplitude of the latter remains an unknown in the model. Periodicity conditions are implemented on the lateral boudaries. For the proposed DG scheme, this is done using the method described in section 3.5.

DOI: 10.1002/nme

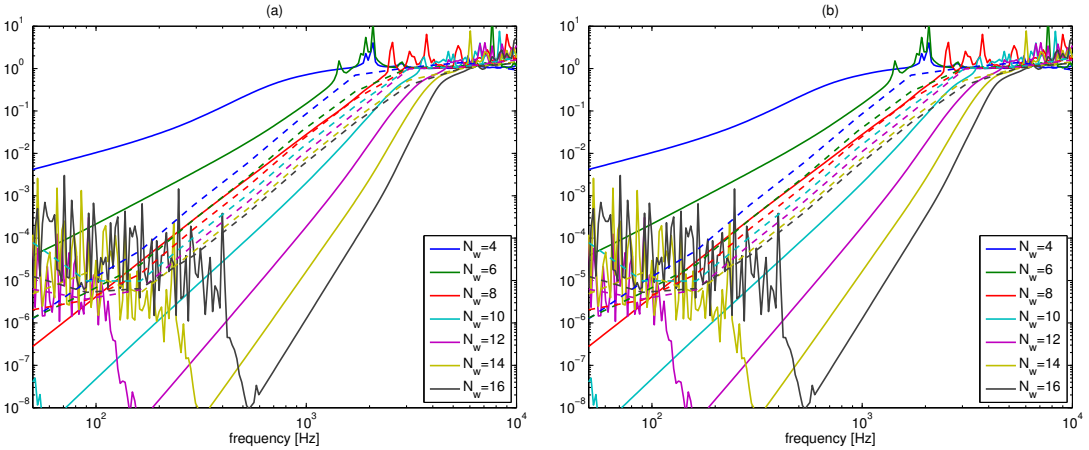

Figure 9. Convergence with frequency: (a) relative L^2 error ε on p_{f} for the first compression wave, (b) relative L^2 error ε on $\mathbf{v}^{\mathrm{s}}$ for the shear wave. Solid lines are DGM results and dashed lines are FEM results. Each color corresponds to a value of N_{w} for DGM and a mesh size for FEM resulting in a similar number of degrees of freedom as DGM. Parameters are $\theta_{\mathrm{s}} = 0$, $h = 0.1$, $\delta\theta = \pi/N_{\mathrm{w}}$.

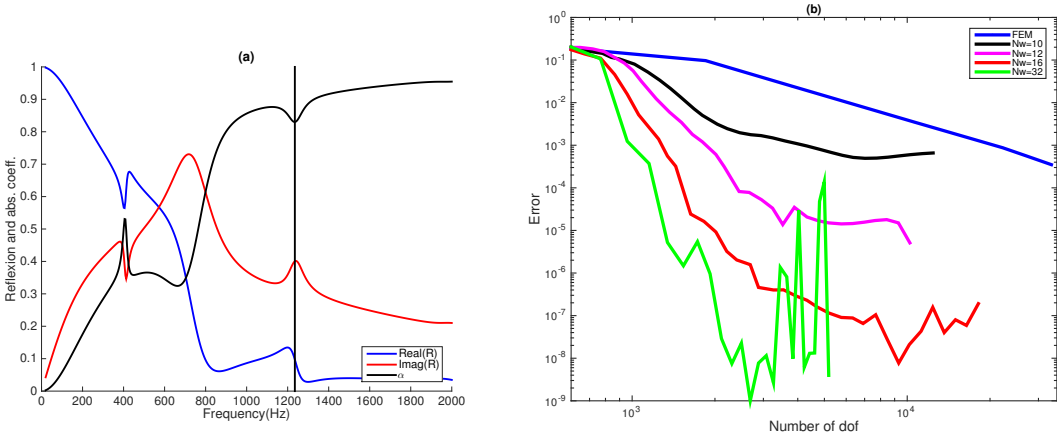

Figure 10. (a) Absorption and reflexion coefficient versus frequency. (b) Relative error on the complex reflexion coefficient.

Figure 10b shows the convergence of the two numerical methods. The relative error on the reflexion coefficient is presented as a function of the number of degrees of freedom. For the FEM, these results are obtained by successive mesh refinements. For the DGM, both the number of plane waves N_{w} and the element size are varied. While the mesh refinement is isotropic for the FEM, for the DGM a single element is used across the thickness of the layer and only the number of elements in the lateral direction is varied. As in the previous test case the DGM exhibits much improved rates of convergence. The convergence for the model with 32 plane waves is very rapid and machine precision is reached with less than 2800 degrees of freedom and then conditioning issues appear. It should be noted that for the DGM the rate of convergence is not fully maintain over the whole range of mesh resolutions and this can be attributed to the aspect ratio of the elements when a large number of elements is used in the lateral direction.

Figure 11 shows the real part of the solutions of the pressure and the x component of the solid displacement, obtained with the FEM and the wave-based DGM. The mesh is displayed for the DGM but not for the FEM as the density of elements is too important to allow for a clear visualisation of the results. The FEM (resp. DGM) model contains 3343 (resp. 1536) degrees of freedom and achieves a relative error of 0.04 (resp. 5e-6). Discrepancies can still be observed on

DOI: 10.1002/nme

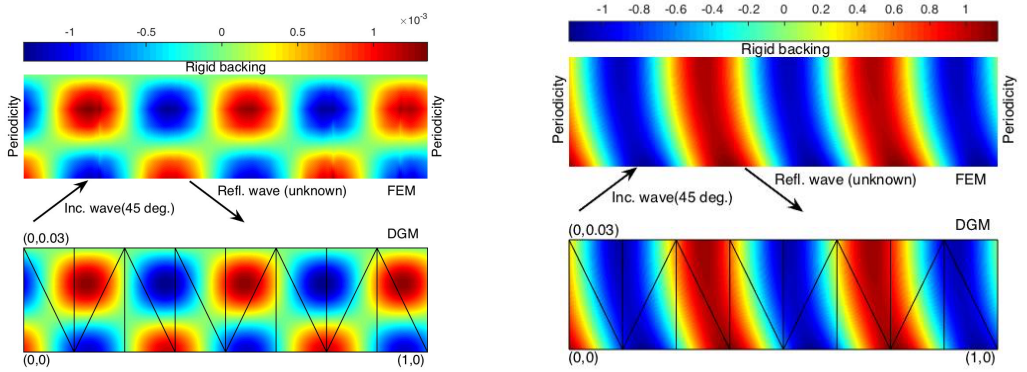

Figure 11. Real part of the solutions of the FEM and the proposed method. (left) solid displacement; (right) pressure

the solid displacement predicted by the FEM while a phase shift can be observed on the pressure field. These results illustrate that the wave-based method can yield accurate results even when large elements, relative to the wavelength, are used.

4.4. Application to the scattering and absorption of sound by a porous cylinder

We now consider a more complex test case, which involves the coupling of waves in air with the waves in a porous material. A cylinder of radius R_0 and made of a poro-elastic material is surrounded by a fluid in which a time-harmonic plane wave with frequency ω is propagating along the x axis. This plane wave is partly reflected by the PEM-air interface and partly transmitted into the porous material where it is rapidly absorbed, as shown in the example solution in figure 12a.

As before the Biot equations (2) are solved in the PEM (for $r < R_0$). The acoustic waves in the surrounding fluid are solution of the Helmholtz equation written in the form (1) with (8).

While this test case includes various features that are important to practical applications (an interface between a PEM and air, sound radiation in free field and curved boundaries), a closed-form analytical solution can be obtained, and a quantitative validation of the numerical model is still possible.

At the interface between the porous material and the surrounding volume of fluid, the two different conditions introduced in section 3.5 are considered. Equation (31) corresponds to the interface conditions required when the fluid is in direct contact with the porous material. Equation (32) describes the case where a thin impermeable film covers the surface of the porous material. It is very common in practical applications to add a porous film on the surface of the PEM in order to adjust its response to acoustic fields. Indeed, the behaviour of a PEM is very sensitive to boundary conditions. Equations (31) and (32) represent the two opposite cases in this context. These two conditions can be formulated in the form of equation (25) and the methodology described in section 3.5 can be readily applied to implement these interface conditions in the variational formulation.

As shown in figure 12b, the computational domain is a disk of radius $3R_0$ discretised using an unstructured triangular mesh. With coarse meshes the circular shape of the scatterer would be poorly approximated by the straight edges of the elements, and this would be the dominating source of numerical error, instead of the plane wave basis. To avoid this the element edges corresponding to the scatterer surface and the outer boundary of the computational domain are treated as arcs rather than straight lines. This implies that on these edges numerical integration is needed to evaluate the element matrices. This represents an additional cost that still remains negligible compared to the whole solution procedure.

On the outer boundary of the domain, sound radiation in free field is formulated by representing the acoustic pressure as a sum of cylindrical harmonics of the form $\mathrm{H}_m^{(2)}(k_0 r)\mathrm{e}^{-\mathrm{i}m\theta}$ where $k_0 = \omega/c_0$.

DOI: 10.1002/nme

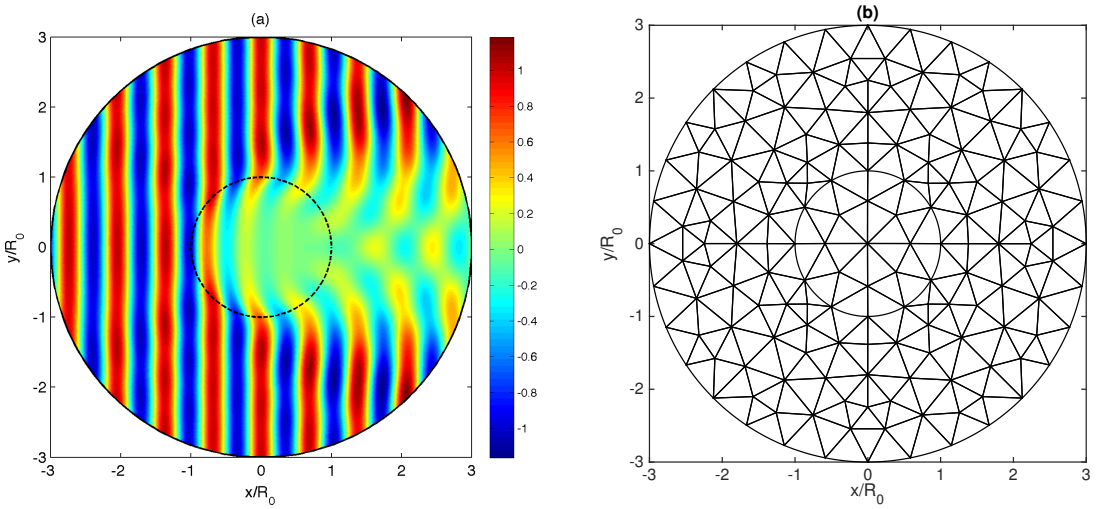

Figure 12. (a) Example of solution p_{f} for $f = 1000\,\mathrm{Hz}$ without the thin film. (b) Example of mesh with $h = 0.6$ for the scattering by a cylinder.

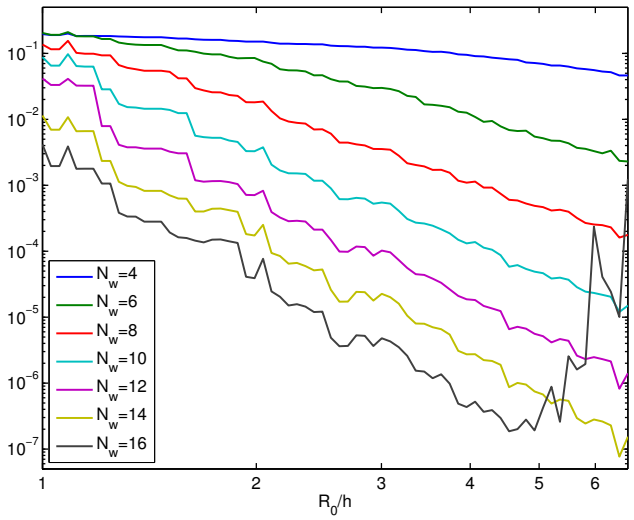

Figure 13. Relative error ε on p_{f} and p_{a} in L^2 norm as a function of the mesh resolution, for the case without thin film at $f = 1000\,\mathrm{Hz}$.

For the results presented here, the properties of the porous material and the air are the same as in the previous section and are given in Appendix A.

Figure 13 shows the convergence of the numerical model as a function of mesh resolution for the case without a thin film. Again the increase in performance when the number of plane waves is increased is clearly observed. As an example, with the coarse mesh shown in figure 12b obtained with $h = 0.45$, the numerical error is brought below $1\,\%$ with just 10 plane waves per element. It is quite significant that such a small model with only 4740 degrees of freedom can represent accurately such a complex sound field. It is only when the numerical error is of the order of $10^{-5}\,\%$ that the poor conditioning of the model has an impact on the accuracy.

A specificity of the proposed method is that within each element the different types of waves supported by the governing equations are represented separately (note however that they are fully coupled at the interfaces between elements and on the boundary of the computational domain). This allows us to consider the contribution of the compression and shear waves in the porous material

DOI: 10.1002/nme

independently. This is shown in figure 14 for the velocity v_x^{t} (rather than pressure which is not influenced by the shear wave).

A first remark on this figure is that for each solution is continuous which shows that each type of waves, taken individually, is discretised in a consistent manner by the numerical model. Secondly it can be observed that the second compression wave which is dominated by the fluid is much more attenuated than the other two. This is expected for most porous materials.

In the case where the porous material is in direct contact with the surrounding fluid, as stated by equation (31), we can see that this second compression wave is three orders of magnitudes larger than the other two types of wave. It is therefore this compression waves which is primarily generated by the incident sound field and that is responsible for the strong absorption of the wave inside the PEM. This illustrates that with equation (31) there is only a weak coupling between the incident acoustic wave and the solid frame of the PEM. In such a situation, an equivalent-fluid model would be well suited to described this problem, and the full Biot equations are not necessarily needed. As a consequence, we could reduce the size of the cost of the wave-based DGM for this problem by using only a plane-wave basis with only the second compression waves.

In contrast, in the case where the PEM is covered by a thin film, equation (32), the wave transmitted into the PEM is weaker due to the inability of the fluid to flow through the film. This is clearly shown by the low amplitude of the velocity in figure 14. Nevertheless, it is interesting to note that the three types of waves now have similar amplitude profiles. In this situation an equivalent-fluid model would not provide adequate predictions as the vibration of the solid frame is as significant as the waves in the fluid. For the wave-based DGM, it is necessary to include all three types of waves in the basis, and including only the second compression waves would not yield accurate results. This highlights that the process of selecting the types and numbers of plane wave in the basis should consider the boundary conditions and that for porous materials criteria based only on wavelength might not be sufficient.

DOI: 10.1002/nme

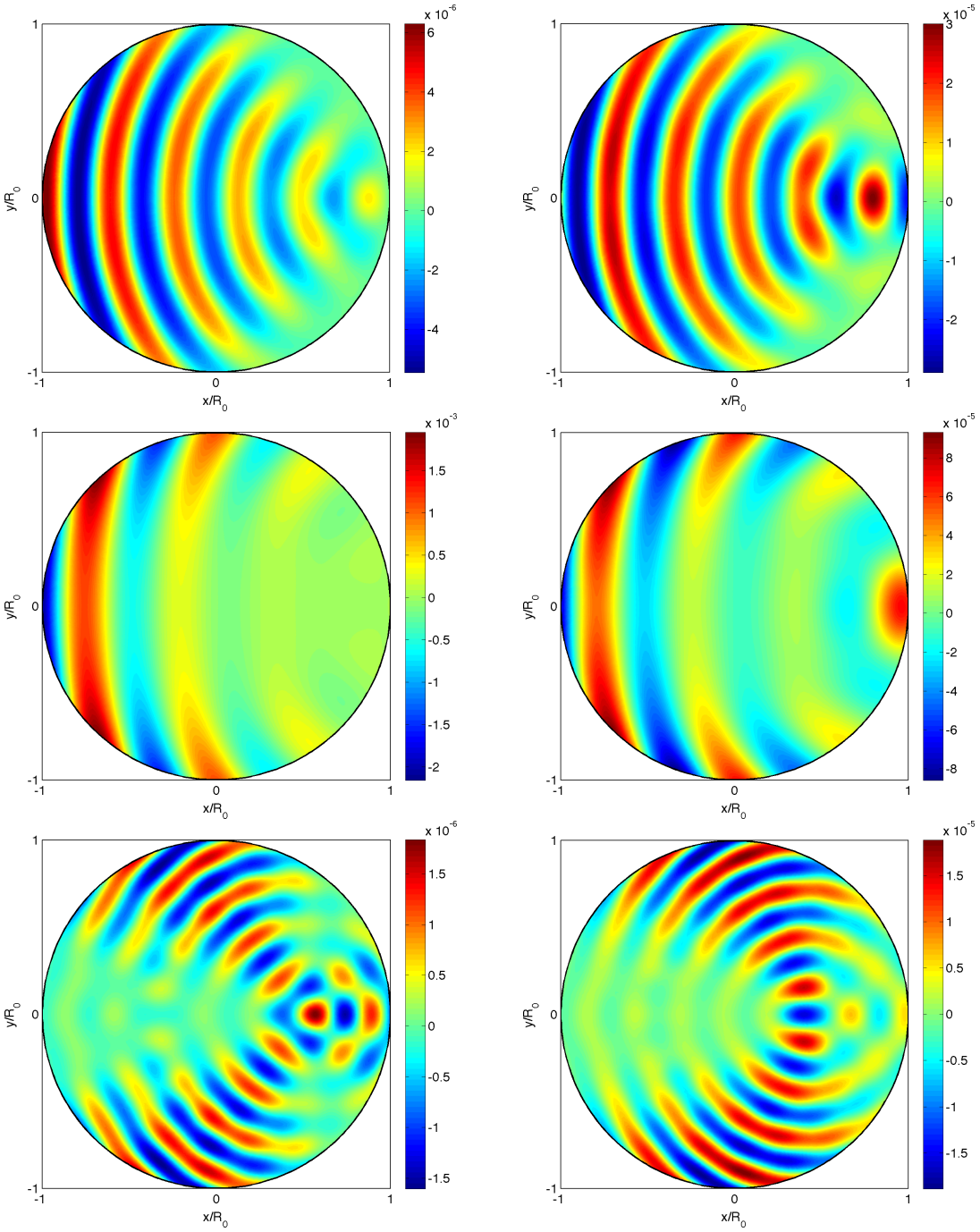

Figure 14. Individual contributions of the three types of waves to the total velocity v_x^{t} in the porous material at $f = 1\,\mathrm{kHz}$: first compression wave (top), second compression wave (center), shear wave (bottom). Left: without thin film. Right: with thin film.

DOI: 10.1002/nme

5. CONCLUSIONS

This paper described the first application of a plane-wave DGM for poroelastic materials modelled using the Biot equations. In a way similar to linear elasticity [33] and aero-acoustics [10], the solution of the Biot equations in each element is described as the sum of different types of waves (in this case two compression waves and a shear wave).

Using the charateristics of the governing equations, a general and systematic procedure was presented to include a large family of boundary conditions and interface conditions in the formulation of the numerical model. This is particularly important in practice since a wide range of coupling conditions between porous materials and air and elastic structures can be found in engineering applications.

The accuracy and efficiency of the method were assessed using different test cases. Results demonstrate the ability of the method to describe accurately complex wave fields with only a small number of degrees of freedom, and to capture the rapid decay of the waves propagating through the porous material. The exponential rate of convergence with the number of plane waves was recovered. Comparison with a quadratic finite element model showed the improved efficiency of the wave-based method, it was observed that the method is more efficient than finite elements if more than 10 plane waves are included in the basis (although a more balanced comparison should consider a high-order finite element method).

As expected with wave-based methods, the conditioning of the numerical model tends to deteriorate when we increase the number of plane waves or reduce the frequency or the element size. Interestingly it was found that the accuracy and the condition number are closely linked. For a fixed accuracy, the condition number increases only slightly when the number of plane waves in the basis is increased. This suggests that it could be possible to control the accuracy of the numerical model by using the condition number. It was found also the conditioning remains acceptable for reasonable levels of accuracy.

The present paper demonstrates the fundamentals of the proposed method and open several perspectives, in particular to tackle realistic 3D problems using the wave-based DGM. The principles of the method are directly applicable to three-dimensional problems, e.g. the variational formulation and the numerical flux. However, a specific challenge is that in practice porous materials are often combined to form a layered acoustic treatment that is attached or glued to a structure. This results in complex, three-dimensional geometries that will require a careful choice of plane-wave bases to maintain the improved efficiency of the method. Also, it might be worth considering hybrid model combining both wave-based elements and standard finite elements. To construct plane wave bases with different types of plane waves, it has been suggested to adjust the relative numbers of waves depending on the wavelength of each type of waves [33, 34]. However results presented in section 4.4 indicate that it would be beneficial also to adjust the number and type of plane waves based on the nature of the boundary conditions.

ACKNOWLEDGEMENT

This work greatly benefited from a Visiting Professor grant from the Université du Maine (Le Mans, France) for G. Gabard.

DOI: 10.1002/nme

A. MATERIAL PROPERTIES

This appendix provides the main expressions needed to define the equivalent parameters of the Biot–Allard model [4]. The values used in this paper for these parameters are listed in table I. These parameters considers both viscous and thermal dissipative mechanisms within the porous material. The density $\widetilde{\rho}_{\mathrm{eq}}$ of the equivalent fluid medium associated to the poroelastic material is

$$\widetilde{\rho}_{\mathrm{eq}} = \frac{\rho_0}{\phi}\widetilde{\alpha}\ , \tag{38}$$

where ϕ is the porosity, ρ_0 is the interstitial fluid density and $\widetilde{\alpha}$ is the dynamic tortuosity defined by:

$$\widetilde{\alpha} = 1 - \frac{\mathrm{i}\phi\sigma}{\alpha_\infty\rho_0\omega}\sqrt{1 - \frac{4\mathrm{i}\alpha_\infty^2\eta_{\mathrm{a}}\rho_0\omega}{(\sigma\Lambda\phi)^2}}\ . \tag{39}$$

In this expression σ is the flow resistivity, η_{a} is the dynamic viscosity of the fluid, α_∞ is the geometric tortuosity and Λ is the viscous characteristic length. The coupling coefficient $\widetilde{\gamma}$ can be obtained from:

$$\widetilde{\gamma} = \frac{\rho_0}{\widetilde{\rho}_{\mathrm{eq}}} - (1 - 2\phi)\ . \tag{40}$$

The solid equivalent densities $\widetilde{\rho}$ and $\widetilde{\rho}_{\mathrm{s}}$ are given by:

$$\widetilde{\rho} = (1-\phi)\rho_{\mathrm{s}} - (\rho_0 - \phi\widetilde{\rho}_{\mathrm{eq}})(2\phi - \rho_0/\widetilde{\rho}_{\mathrm{eq}})\ , \quad \text{and } \widetilde{\rho}_{\mathrm{s}} = \widetilde{\rho} - \widetilde{\gamma}^2\widetilde{\rho}_{\mathrm{eq}}\ , \tag{41}$$

where ρ_{s} is skeleton material density.

The thermal properties are given by the dynamic compressibility $\widetilde{K}_{\mathrm{eq}}$:

$$\widetilde{K}_{\mathrm{eq}} = \gamma p_0 \Big/ \left[\gamma - (\gamma-1)\Big/\left(1 + \frac{8\eta_{\mathrm{a}}}{\mathrm{i}\omega\rho_0\mathrm{Pr}\Lambda'}\sqrt{1 + \frac{\mathrm{i}\omega\rho_0\mathrm{Pr}\Lambda'^2}{16\eta_{\mathrm{a}}}}\right)\right]\ , \tag{42}$$

where Λ' is the thermal characteristic length, Pr is the Prandtl number, p_0 is the ambient pressure, γ is the ratio of specific heats of air.

The structural mechanical parameters N and $\hat{A}$ are given by:

$$N = \frac{E(1+\mathrm{i}\eta_{\mathrm{s}})}{2(1+\nu)}\ , \quad \hat{A} = \frac{2N\nu}{1-2\nu}\ . \tag{43}$$

where E is the in-vacuo Young's modulus, η_{s} is the loss factor of the frame and ν is the Poisson coefficient.

Finally the sound speed in the fluid is given by $c_0 = \gamma p_0/\rho_0$.

Parameter	Unit	Mat A	Mat B
ϕ	[1]	0.98	0.98
σ	$[\mathrm{N\,s\,m^{-4}}]$	15500	45000
α_∞	[1]	1.01	1.00
Λ	[μm]	100	100
Λ'	[μm]	200	250
ρ_{s}	$[\mathrm{kg/m^3}]$	11	23
E	[Pa]	200E3	140E3
ν	[1]	0.35	0.24
η_{s}	[1]	0.1	0.05

Table I. Properties of the porous material.

DOI: 10.1002/nme

B. DETAILED EXPRESSIONS FOR THE BIOT EQUATIONS

The matrix of eigenvalues $\mathbf{\Lambda}$ is

$$\mathbf{\Lambda} = \mathrm{diag}(0, 0, -c_1, -c_2, -c_3, c_1, c_2, c_3) \ ,$$

where the phase velocities c_i of the three different types of waves are given by

$$c_i^2 = \frac{2\omega^2}{\left(\delta_{\mathrm{s}2}^2 + \delta_{\mathrm{eq}}^2\right) \pm \sqrt{\left(\delta_{\mathrm{s}2}^2 + \delta_{\mathrm{eq}}^2\right)^2 - 4\delta_{\mathrm{eq}}^2\delta_{\mathrm{s}1}^2}} \ , \text{ for } i = 1, 2 \ , \quad \text{and } c_3^2 = \frac{N}{\widetilde{\rho}} \ ,$$

with $i = 1$ and 2 correspond to the first and second compression waves and $i = 3$ to the shear wave. In the expression above we have used the wave number δ of these waves

$$\delta_{\mathrm{eq}} = \omega\sqrt{\frac{\widetilde{\rho}_{\mathrm{eq}}}{\widetilde{K}_{\mathrm{eq}}}} \ , \quad \delta_{\mathrm{s}1} = \omega\sqrt{\frac{\widetilde{\rho}}{\hat{P}}} \ , \quad \delta_{\mathrm{s}2} = \omega\sqrt{\frac{\widetilde{\rho}_{\mathrm{s}}}{\hat{P}}} \ .$$

The corresponding matrix of eigenvectors can be written $\mathbf{P} = [\mathbf{P}^0\, \mathbf{P}^+\, \mathbf{P}^-]$ with

$$\mathbf{P}^0 = \begin{bmatrix} 0 & 0 \\ 0 & 0 \\ n_y & 0 \\ -n_x & 0 \\ 0 & 1 \\ 0 & -2n_xn_y \\ 0 & n_y^2 - n_x^2 \\ 0 & 0 \end{bmatrix} \ , \quad \mathbf{P}^+ = \begin{bmatrix} n_x & n_x & n_y \\ n_y & n_y & -n_x \\ \mu_1 n_x & \mu_2 n_x & \mu_3 n_y \\ \mu_1 n_y & \mu_2 n_y & -\mu_3 n_x \\ -\frac{\hat{A}+2N}{2c_1} & -\frac{\hat{A}+2N}{2c_2} & 0 \\ -\frac{2N}{c_1} n_x n_y & -\frac{2N}{c_2} n_x n_y & \frac{N}{c_3}(n_x^2 - n_y^2) \\ -\frac{N}{c_1}(n_x^2 - n_y^2) & -\frac{N}{c_2}(n_x^2 - n_y^2) & -\frac{2N}{c_3} n_x n_y \\ \frac{\mu_1}{c_1}\tilde{K}_{\mathrm{eq}} & \frac{\mu_1}{c_2}\tilde{K}_{\mathrm{eq}} & 0 \end{bmatrix} \ , \tag{44}$$

with

$$\mu_i = \widetilde{\gamma}\frac{(\delta_i^2 - \delta_{\mathrm{s}2}^2)}{\delta_{\mathrm{s}2}^2 - \delta_{\mathrm{s}1}^2} \ , \text{ for } i = 1, 2 \ , \quad \text{and } \mu_3 = -\widetilde{\gamma} \ .$$

$\mathbf{P}^-$ is obtained by substituting n_x and n_y by $-n_x$ and $-n_y$ in the expression for $\mathbf{P}^+$.

Similarly the inverse of the matrix $\mathbf{Q}$ of $\mathbf{P}$ can be written $\mathbf{Q} = [\mathbf{Q}^0\, \mathbf{Q}^+\, \mathbf{Q}^-]^T$ with

$$\mathbf{Q}^+ = \frac{1}{2(\mu_2 - \mu_1)} \begin{bmatrix} \mu_2 n_x & -\mu_1 n_x & n_y(\mu_2 - \mu_1) \\ \mu_2 n_y & -\mu_2 n_y & -n_x(\mu_2 - \mu_1) \\ n_x & n_x & 0 \\ n_y & n_y & 0 \\ -\frac{\mu_2 c_1}{\hat{A}+2N} & \frac{\mu_1 c_2}{\hat{A}+2N} & 0 \\ -\frac{n_x n_y \mu_2 c_1}{N} & \frac{n_x n_y \mu_1 c_2}{N} & \frac{(n_x^2 - n_y^2)c_3(\mu_2 - \mu_1)}{N} \\ -\frac{\mu_2(n_x^2 - n_y^2)c_1}{2N} & \frac{\mu_1(n_x^2 - n_y^2)c_2}{2N} & \frac{-2n_x n_y c_3(\mu_2 - \mu_1)}{N} \\ \frac{c_1}{\widetilde{K}_{\mathrm{eq}}} & \frac{c_2}{\widetilde{K}_{\mathrm{eq}}} & 0 \end{bmatrix} \ ,$$

$$\mathbf{Q}^0 = \frac{1}{2(\mu_2 - \mu_1)} \begin{bmatrix} -\mu_3 n_y & 0 \\ \mu_3 n_x & 0 \\ n_y & 0 \\ -n_x & 0 \\ 0 & 1 \\ 0 & -2n_x n_y \\ 0 & n_y^2 - n_x^2 \\ 0 & 0 \end{bmatrix} \ .$$

The expression for $\mathbf{Q}^-$ is obtained by substituting n_x and n_y by $-n_x$ and $-n_y$ in the expression for $\mathbf{Q}^+$.

Prepared using nmeauth.cls
DOI: 10.1002/nme

C. DETAILED EXPRESSIONS FOR THE WAVE EQUATION

The eigenvalues of the flux matrix $\mathbf{F}$

$$\mathbf{\Lambda} = \mathrm{diag}(0, c_0, -c_0) \ .$$

The corresponding matrix of eigenvectors of $\mathbf{F}$ and its inverse are

$$\mathbf{P} = \begin{bmatrix} 0 & c_0 & c_0 \\ n_y & n_x & -n_x \\ -n_x & n_y & -n_y \end{bmatrix} \ , \quad \mathbf{Q} = \frac{1}{2} \begin{bmatrix} 0 & 2n_y & -2n_x \\ 1/c_0 & n_x & n_y \\ 1/c_0 & -n_x & -n_y \end{bmatrix} \ .$$

DOI: 10.1002/nme

REFERENCES

1. Biot MA. Theory of propagation of elastic waves in a fluid-saturated porous solid. I. low-frequency range. *The Journal of the Acoustical Society of America* 1956; **28**(2):168–178.
2. Johnson DL, Koplik J, Dashen R. Theory of dynamic permeability and tortuosity in fluid-saturated porous media. *Journal of Fluid Mechanics* 1987; **176**:379–402.
3. Champoux Y, Allard JF. Dynamic tortuosity and bulk modulus in air-saturated porous media. *Journal of Applied Physics* 1991; **70**(4):1975–1979.
4. Allard J, Atalla N. *Propagation of Sound in Porous Media: Modelling Sound Absorbing Materials*. John Wiley & Sons, 2009.
5. Hesthaven JS, Warburton T. *Nodal discontinuous Galerkin methods: algorithms, analysis, and applications*. Springer, 2007.
6. Melenk J, Babuška I. The partition of unity finite element method: Basic theory and applications. *Computer Methods in Applied Mechanics and Engineering* 1996; **139**:289–314.
7. Cessenat O, Després B. Application of an ultra weak variational formulation of elliptic PDEs to the two-dimensional Helmholtz problem. *SIAM Journal in Numerical Analysis* 1998; **35**:255–299.
8. Farhat C, Harari I, Franca LP. The discontinuous enrichment method. *Computer methods in applied mechanics and engineering* 2001; **190**(48):6455–6479.
9. Farhat C, Harari I, Hetmaniuk U. A discontinuous Galerkin method with Lagrange multipliers for the solution of Helmholtz problems in the mid-frequency regime. *Computer Methods in Applied Mechanics and Engineering* 2003; **192**(11):1389–1419.
10. Gabard G. Discontinuous Galerkin methods with plane waves for time-harmonic problems. *Journal of Computational Physics* 2007; **225**:1961–1984.
11. Gittelson C, Hiptmair R, Perugia I. Plane wave discontinuous Galerkin methods: analysis of the h-version. *ESAIM: Mathematical Modelling and Mumerical Analysis* 2009; **43**:297–331.
12. Hiptmair R, Moiola A, Perugia I. Plane wave discontinuous Galerkin methods for the 2d Helmholtz equation: analysis of the p-version. *SIAM Journal of Numerical Analysis* 2011; **49**(1):264–284.
13. Hiptmair R, Moiola A, Perugia I. Error analysis of Trefftz-discontinuous Galerkin methods for the time-harmonic maxwell equations. *Mathematics of Computation* 2013; **82**(281):247–268.
14. Gittelson CJ, Hiptmair R. Dispersion analysis of plane wave discontinuous Galerkin methods. *International Journal for Numerical Methods in Engineering* 2014; **98**(5):313–323.
15. Huttunen T, Malinen M, Monk P. Solving Maxwell's equations using the ultra weak variational formulation. *Journal of Computational Physics* 2007; **223**(2):731–758.
16. Gabard G, Gamallo P, Huttunen T. A comparison of wave-based discontinuous Galerkin, ultra-weak and least-square methods for wave problems. *International Journal for Numerical Methods in Engineering* 2011; **85**:380–402.
17. Monk P, Wang DQ. A least-squares method for the Helmholtz equation. *Computer Methods in Applied Mechanics and Engineering* 1999; **175**:121–136.
18. Deckers E, Van Genechten B, Vandepitte D, Desmet W. Efficient treatment of stress singularities in poroelastic wave based models using special purpose enrichment functions. *Computers & Structures* 2011; **89**(11):1117–1130.
19. Deckers E, Hörlin NE, Vandepitte D, Desmet W. A wave based method for the efficient solution of the 2D poroelastic Biot equations. *Computer Methods in Applied Mechanics and Engineering* 2012; **201**:245–262.
20. Lähivaara T, Huttunen T. A non-uniform basis order for the discontinuous Galerkin method of the 3D dissipative wave equation with perfectly matched layer. *Journal of Computational Physics* 2010; **229**(13):5144–5160.
21. Chazot J, Nennig B, Perrey-Debain E. Performances of the partition of unity finite element method for the analysis of two-dimensional interior sound fields with absorbing materials. *Journal of Sound and Vibration* 2013; **332**(8):1918–1929.
22. Chazot J, Perrey-Debain E, Nennig B. The partition of unity finite element method for the simulation of waves in air and porous media. *Journal of the Acoustical Society of America* 2014; **135**(2):724–733.
23. Dazel O, Brouard B, Depollier C, Griffiths S. An alternative Biot's displacement formulation for porous materials. *Journal of the Acoustical Society of America* 2007; **121**(6):3509–3516.
24. Whitham G. *Linear and nonlinear waves*. Wiley-Interscience, 1999.
25. Leveque R. *Finite volume methods for hyperbolic problems*. Cambridge University Press, 2002.
26. Kreiss H. Initial boundary value problems for hyperbolic systems. *Communications on Pure and Applied Mathematics* 1970; **23**:277–298.
27. Higdon R. Initial-boundary value problems for linear hyperbolic systems. *SIAM Review* 1986; **28**(2):177–217.
28. Moiola A. Approximation properties of plane wave spaces and application to the analysis of the plane wave discontinuous Galerkin method. *Technical Report 2009-06*, ETH Zürich, Seminar für Angewandte Mathematik 2009.
29. Atalla N, Panneton R, Debergue P. A mixed displacement-pressure formulation for poroelastic materials. *Journal of the Acoustical Society of America* 1998; **104**(3):1444–1452.
30. Atalla N, Hamdi M, Panneton R. Enhanced weak integral formulation for the mixed (u, p) poroelastic equations. *Journal of the Acoustical Society of America* 2001; **109**(6):3065–3068.
31. Göransson P. A 3d, symetric finite element formulation of the Biot equations with application to acoustic wave propagation through an elastic porous medium. *International Journal for Numerical Methods in Engineering* 1998; **41**:167–192.
32. Hörlin N, Nordström M, Göransson P. A 3-D hierarchical FE formulation of Biot's equations for elasto-acoustic modelling of porous media. *Journal of Sound and Vibration* 2001; **243**(4):633–652.
33. Huttunen T, Monk P, Collino F, Kaipio J. The ultra-weak variational formulation for elastic wave problems. *SIAM Journal in Scientific Computing* 2004; **25**(5):1717–1742.

DOI: 10.1002/nme

34. El Kacimi A, Laghrouche O. Improvement of PUFEM for the numerical solution of high-frequency elastic wave scattering on unstructured triangular mesh grids. *International Journal for Numerical Methods in Engineering* 2010; **84**(3):330–350.

DOI: 10.1002/nme